



City Research Online

City, University of London Institutional Repository

Citation: Naseri, H., Koukouvinis, P., Malgarinos, I. & Gavaises, M. (2018). On viscoelastic cavitating flows: A numerical study. *Physics of Fluids*, 30(3), 033102. doi: 10.1063/1.5011978

This is the accepted version of the paper.

This version of the publication may differ from the final published version.

Permanent repository link: <https://openaccess.city.ac.uk/id/eprint/19438/>

Link to published version: <https://doi.org/10.1063/1.5011978>

Copyright: City Research Online aims to make research outputs of City, University of London available to a wider audience. Copyright and Moral Rights remain with the author(s) and/or copyright holders. URLs from City Research Online may be freely distributed and linked to.

Reuse: Copies of full items can be used for personal research or study, educational, or not-for-profit purposes without prior permission or charge. Provided that the authors, title and full bibliographic details are credited, a hyperlink and/or URL is given for the original metadata page and the content is not changed in any way.

City Research Online:

<http://openaccess.city.ac.uk/>

publications@city.ac.uk

1 **On viscoelastic cavitating flows: A numerical study**

2
3 Homa Naseri, Phoevos Koukouvinis, Ilias Malgarinos and Manolis Gavaises

4
5 School of Mathematics, Computer Science & Engineering, City, University of London,
6 London, Northampton Square, EC1V 0HB, UK

7
8 Keywords:

9 Cavitation, Viscoelasticity, Phan-Thien-Tanner Fluid

10 11 **Abstract**

12 The effect of viscoelasticity on turbulent cavitating flow inside a nozzle is simulated for
13 Phan-Thien-Tanner (PTT) fluids. Two different flow configurations are used to show the
14 effect of viscoelasticity on different cavitation mechanisms, namely cloud cavitation
15 inside a step nozzle and string cavitation in an injector nozzle.

16 In incipient cavitation condition in the step nozzle, small-scale flow features including
17 cavitating microvortices in the shear layer, are suppressed by viscoelasticity. Flow
18 turbulence and mixing is weaker compared to the Newtonian fluid, resulting in
19 suppression of microcavities shedding from the cavitation cloud. Moreover, mass
20 flowrate fluctuations and cavity shedding frequency are reduced by the stabilizing effect
21 of viscoelasticity. Time averaged values of the liquid volume fraction show that
22 cavitation formation is strongly suppressed in the PTT viscoelastic fluid, and the cavity
23 cloud is pushed away from the nozzle wall.

24 In the injector nozzle, a developed cloud cavity covers the nozzle top surface while a
25 vortex-induced string cavity emerges from the turbulent flow inside the sac volume.
26 Similar to the step nozzle case, viscoelasticity reduces the vapor volume fraction in the
27 cloud region. However, formation of the streamwise string cavity is stimulated as
28 turbulence is suppressed inside the sac volume and the nozzle orifice. Vortical
29 perturbations in the vicinity of the vortex are damped allowing more vapor to develop in
30 the string cavity region. The results indicate that the effect of viscoelasticity on
31 cavitation depends on the alignment of the cavitating vortices with respect to the main
32 flow direction.

33 1. Introduction

34 Cavitation dynamics and control is the subject of ongoing research with applications in
35 pumps and propellers¹⁻³, injector nozzles⁴⁻⁶ and medicine⁷⁻⁹. In nozzle flows, cavitation
36 vapors block the effective flow passage area, significantly reducing the nozzle
37 discharge coefficient¹⁰⁻¹³. Computational fluid dynamics (CFD) studies and X-rays of
38 cavitating flows can directly show the reduction of fluid density in a nozzle due to
39 cavitation^{4,6,14-17}. Fully compressible simulations of cavitating nozzle flows can reveal
40 that pressure waves produced during the bubble collapse events increase the jet
41 instabilities and promote the primary jet breakup¹⁷.

42 Fluid properties can affect the in-nozzle flow by modifying the flow turbulence and
43 cavitation. This is because formation and collapse of cavitation vapors is subject to
44 pressure fluctuations due to local flow instabilities and a two-way interaction exists
45 between cavitation and turbulence. Moreover, collapse of cavitation bubbles is a
46 primary mechanism for vorticity production and enhancement of streamwise velocity
47 fluctuations¹⁸⁻²¹. Compression and expansion of cavitation vapors results in
48 misalignment of the density gradients and the pressure gradients, hence the baroclinic
49 torque (the source term $e_{ijk} \frac{\partial \rho}{\partial x_j} \frac{\partial p}{\partial x_k} / \rho^2$ appearing in the vorticity transport equation) is
50 increased, producing vorticity^{19,20}. Time-resolved X-ray densitometry of cavitation void-
51 fraction in a cavity cloud²² has identified that in addition to the re-entrant jet motion,
52 bubbly shock propagation due to reduction of speed of sound in the mixture region, is
53 responsible for the shedding of the cavitation cloud. More recently, high speed phase
54 contrast imaging using synchrotron radiation has been used to provide details on the
55 temporal evolution of cavitating vortices²³.

56 In addition to compressibility effects, cavitation also modifies the size and shape of the
57 vortical structures in the flow and hence the interaction between the small and large

58 scales. Experimental analysis using PIV-LIF in a cavitating mixing layer has shown a
59 reduction in the size of the coherent vortices as cavitation intensifies²¹. Turbulence
60 anisotropy is increased as cavitation enhances the diffusivity in the streamwise
61 direction while damping the cross-stream diffusivity²¹. Moreover, bubbles in vortex
62 rings can distort and elongate an initially circular vortex core, as the bubble volume
63 forces (pressure gradient, viscous and buoyancy forces) change the momentum in the
64 liquid phase²⁴.

65 Compared to single-phase fluids, bubbly mixtures have different bulk properties such
66 as viscosity, density and compressibility which modify the turbulent flow dynamics²⁵.
67 Injection of gas bubbles can provide lubrication for external liquid flows and a great
68 body of research is dedicated to understanding the mechanism of drag reduction in
69 bubbly flows²⁵⁻³⁰. The near-wall population of bubbles is an important factor for drag
70 reduction, as the bubbles located in the buffer layer region can interact and modify the
71 streamwise vortices²⁵. Bubbles create a lift force in the wall-normal direction which
72 disrupts the flux of energy from the large scales to the dissipative scales²⁷.

73 Viscosity and elasticity of bubbly mixtures contribute to the resistance of such mediums
74 to deformation in fluid flow³¹. In fact bubbly liquids can be modelled using constitutive
75 equations to describe their viscoelastic properties³². However, not much is known
76 about the effect of viscoelasticity in turbulent cavitating flows and studies discussing
77 viscoelastic properties in turbulent flows mainly focus on turbulent drag reduction.

78 Turbulent drag reduction by viscoelastic additives was first discovered by Toms³³ in
79 1948, since then it has been numerically and experimentally studied extensively³⁴⁻⁴⁸.
80 Modification of fluid properties and flow turbulence is achieved even using very dilute
81 solutions of high molecular weight polymers⁴⁹ or surfactant systems⁵⁰. This knowledge
82 is applied in oil delivery pipelines or district heating/cooling systems to reduce the
83 turbulent drag, heat losses and the pumping costs^{51,52}.

84 The drag reduction mechanism in viscoelastic fluids is related to the interaction
85 between the polymers and turbulence. Polymer viscosity as well as polymer elasticity,
86 measured in terms of relaxation time, are both shown to be effective in this mechanism;
87 however viscosity and elasticity effects form the basis for two theories describing drag
88 reduction⁴³. In the theory based on polymer viscosity, stretching of the polymers
89 increases the total viscosity, suppressing the Reynolds stresses in the buffer layer
90 region. As a result the thickness of the viscous sub-layer is increased and the turbulent
91 drag is reduced ^{43,53-55}. In the elastic theory, the onset of drag reduction is when the
92 elastic energy in the polymers becomes comparable to the Reynolds stresses in the
93 buffer layer at length scales larger than the Kolmogorov scale. Consequently the
94 energy cascade is truncated as the small-scales are suppressed and the viscous
95 sublayer is thickened resulting in drag reduction ^{43,56}.

96 Literature studies that correlate viscoelasticity and cavitation mainly focus on bubble
97 dynamics in viscoelastic tissue-like medium. Microbubbles can act as ultrasound
98 contrast agents⁵⁷ and bubble cluster collapse events can be used to destroy kidney
99 stones (lithotripsy)⁵⁸ and malignant tissue (histotripsy)⁵⁸. Viscoelasticity inhibits the high
100 velocity liquid jet formed during the bubble collapse⁵⁹⁻⁶³ and reduces the pressure
101 amplitudes of acoustic emissions in ultrasound induced cavitation^{61,64}. Viscous effects
102 inhibit large bubble deformations and prevent incoherent bubble oscillations ⁶². In a
103 viscoelastic fluid, bubble oscillations can be damped by viscosity and compressibility
104 effects, however at large elasticity values viscous damping becomes almost negligible
105 and mainly compressibility effects are important⁶⁵. When elasticity effects are small,
106 viscous damping is more dominant but compressibility can also have a substantial
107 contribution to the damping mechanism⁶⁵ and should be accounted for in strong
108 collapse events⁶⁶.

109 Bubble oscillations are enhanced when the relaxation time of the viscoelastic media is
110 increased⁶⁵⁻⁶⁷. At high relaxation times, bubble motion is more violent and less
111 damped, resulting in higher bubble growth rates⁶⁶. This is because when elasticity is
112 high, the surrounding fluid behaves like an inviscid medium, whereas for low relaxation
113 times (negligible elasticity) the behavior of the surrounding fluid is Newtonian⁶⁶.

114 Flow rotation and recirculation regions regularly appear in practical flow conditions
115 where pre-existing bubbles and nuclei are convected into areas of low pressure. In
116 swirling flow conditions, cavitation inception can happen in the low pressure core of
117 large scale vortices forming in regions of high vorticity. This phase change mechanism
118 is known as “vortex cavitation”⁶⁸ and it can appear in propellers, turbines and hydrofoils
119 as well as inside the fuel injector nozzles where it is referred to as “string cavitation”
120^{69,70}. Geometric constrictions such as sharp turns at a nozzle entrance¹⁴ or a venturi
121 throat²⁰, also generate flow instabilities that produce clouds of vapor. “Cloud cavitation”
122 regions are characterized by a re-entrant jet motion and the periodic growth and
123 shedding of the vapor clouds⁷¹. Injection of polymers can be effective in delaying the
124 tip vortex cavitation in marine propellers⁷² as the pressure fluctuations in the cavitation
125 inception region are suppressed⁷³. However studies on interaction of viscoelasticity and
126 cavitation are scarce in the literature.

127 This study aims to provide an understanding about the effect of viscoelasticity on
128 cavitating flows and demonstrate some of the physical aspects of this type of flow. In
129 particular, the effect of viscoelasticity on vapor production in cloud cavitation and string
130 cavitation mechanisms in turbulent flow conditions is investigated in two different
131 injector configurations. As it was discussed earlier, viscoelasticity can alter flow
132 turbulence and bubble dynamics, hence cavitation inception and development are also
133 expected to be altered in viscoelastic fluids due to the two-way interaction between
134 cavitation and turbulence.

135 Numerical simulations of the Navier-Stokes equations are performed using the finite
136 volume method for the flow through a step nozzle in incipient cavitation condition and in
137 an injector nozzle that has both cloud cavitation and string cavitation structures.
138 Instantaneous and time-averaged flow and cavitation structures demonstrate the
139 differences between the inception and development of cavitation structures in
140 Newtonian and viscoelastic fluids.

141 **2. Numerical framework and setup**

142 Flow turbulence can be most accurately described using direct numerical simulations
143 (DNS), however this requires capturing the sharp interface between different phases
144 and a grid size set to the smallest flow scales (Kolmogorov scale) which is not currently
145 affordable. Alternatively, large eddy simulations (LES) can capture the large scale
146 instabilities and vortical structures involved in inception and shedding of cavitation
147 vapors and can be used for practical cases. The Phan-Thien-Tanner model ⁷⁴ is used
148 to model the viscoelastic fluid, which provides a constitutive equation taking into
149 account the polymers microstructure. This model is based on a network theory and
150 assumes that polymer junctions constantly break and reform, so unlike viscoelastic
151 models that consider the polymers to act as elastic beads and spring dumbbells, the
152 PTT polymer network has a dynamic nature. Moreover, the PTT model has also been
153 used to predict the viscoelastic flow behavior in dilute polymer solutions ^{75,76}.

154 To model the multiphase flow the mixture model is used which assumes a
155 homogeneous two phase flow where the mixture density ρ_m is computed from the vapor
156 volume fraction α :

$$157 \quad \rho_m = \alpha\rho_v + (1 - \alpha)\rho_l \quad (1)$$

158 where ρ_v and ρ_l are the vapor and the liquid densities respectively and the vapor
 159 volume fraction α is calculated from the cavitation model presented in equation (7).

160 The mass and momentum conservation equations for the mixture are:

$$161 \quad \frac{\partial \rho_m}{\partial t} + \frac{\partial(\rho_m \mathbf{u}_i)}{\partial x_i} = 0 \quad (2)$$

$$162 \quad \frac{\partial \rho_m \mathbf{u}_i}{\partial t} + \frac{\partial(\rho_m \mathbf{u}_i \mathbf{u}_j)}{\partial x_j} = -\frac{\partial p}{\partial x_i} + \frac{\partial}{\partial x_j} \left(\mu_{\text{eff}} \left(\frac{\partial \mathbf{u}_i}{\partial x_j} + \frac{\partial \mathbf{u}_j}{\partial x_i} \right) \right) + \frac{\partial \tau_{ij}}{\partial x_i} \quad (3)$$

163 The last term in the momentum equation represents the source term from the
 164 viscoelastic stress contribution. μ_{eff} is the effective viscosity which is the molecular
 165 viscosity plus the turbulent viscosity.

166 Flow turbulence is modelled using the wall-adapting local eddy viscosity (WALE) model
 167 developed for wall-bounded flows⁷⁷ where the eddy viscosity is a function of both local
 168 strain rate and rotation rate:

$$169 \quad \mu_t = \rho L_s^2 \frac{(\mathbf{S}_{ij}^d \mathbf{S}_{ij}^d)^{3/2}}{(\mathbf{S}_{ij} \mathbf{S}_{ij})^{5/2} + (\mathbf{S}_{ij}^d \mathbf{S}_{ij}^d)^{5/4}} \quad (4)$$

170 The spatial operator $L_s = \min(d, C_w U^{1/3})$ is defined based of the distance from the wall
 171 and $C_w = 0.325$, so the eddy viscosity predicts the correct y^3 near-wall asymptote and
 172 naturally goes to zero at the wall. \mathbf{S}_{ij} is the strain rate tensor and \mathbf{S}_{ij}^d is the deformation
 173 tensor:

$$174 \quad \mathbf{S}_{ij} = \frac{1}{2} \left(\frac{\partial \mathbf{u}_i}{\partial x_j} + \frac{\partial \mathbf{u}_j}{\partial x_i} \right) \quad (5)$$

175
$$\mathbf{s}_{ij}^d = \frac{1}{2} \left[\left(\frac{\partial \mathbf{u}_i}{\partial x_j} \right)^2 + \left(\frac{\partial \mathbf{u}_j}{\partial x_i} \right)^2 \right] - \frac{1}{3} \text{tr} \left[\left(\frac{\partial \mathbf{u}_i}{\partial x_j} \right)^2 \right] \delta_{ij} \quad (6)$$

176 And δ_{ij} is the Kronecker delta.

177 The cavitation model of Schnerr and Sauer ⁷⁸ is employed which solves a transport
 178 equation for the vapor volume fraction α using a mass transfer rate equation based on
 179 the Rayleigh-Plesset equation for bubble dynamics:

180
$$\frac{\partial}{\partial t} (\alpha \rho_v) + \frac{\partial (\alpha \rho_v \mathbf{u}_i)}{\partial x_i} = \frac{\rho_v \rho_l}{\rho_m} \alpha (1 - \alpha) \frac{3}{\Re_B} \left(\sqrt{\frac{2}{3} \frac{|p_v - p|}{\rho_l}} \right) \text{sign}(p_v - p) \quad (7)$$

181 p_v is the vapor pressure, p is the local pressure and \Re_B is the bubble radius taken as
 182 10^{-6} m which is a few orders of magnitude smaller than the cell size inside the nozzles.
 183 Reducing the bubble radius too much will push the mass transfer rate to infinity as the
 184 phase change process tends toward thermodynamic equilibrium, however this will also
 185 destabilize the solution.

186 Prediction of cavitation using mass transfer rate models has been quantitatively
 187 validated by the authors recently using X-ray micro-CT measurements of vapor volume
 188 fraction⁶ inside an orifice. By considering a mass transfer rate between the two phases,
 189 the liquid/vapor mixture becomes compressible even if the pure phases are treated as
 190 incompressible and the mass transfer rate is the dominant term affecting the sonic
 191 velocity of the mixture⁷⁹. Moreover, as the mass transfer rate tends to infinity the model
 192 moves toward thermodynamic equilibrium and tends asymptotically to a barotropic
 193 cavitation model.

194 The PTT constitutive model ⁷⁴ assumes that the fluid element contains several polymer
 195 junctions which can move by polymer extension and relaxation and the rate of “creation
 196 and destruction” of the junctions is determined from the strain rate tensor:

197
$$\lambda \overset{\nabla}{\tau}_{ij} + f(\text{tr}(\tau_{ij})) \cdot \tau_{ij} = \mu_p \left(\frac{\partial \mathbf{u}_i}{\partial x_j} + \frac{\partial \mathbf{u}_j}{\partial x_i} \right) \quad (8)$$

198 where τ_{ij} is the viscoelastic stress, μ_p is the polymer viscosity and $f(\text{tr}(\tau_{ij}))$ is:

199
$$f(\text{tr}(\tau_{ij})) = 1 + \varepsilon \frac{\lambda}{\mu_p} (\text{tr}(\tau_{ij})) \quad (9)$$

200 where λ is the polymer relaxation time and the extensibility factor ε is 0.02 for dilute
 201 solutions⁸⁰. For $\varepsilon \rightarrow 0$ the Oldroyd-B model is recovered and both of these models
 202 have been widely used in the literature to fit the experimental data of viscoelastic fluids.

203 $\overset{\nabla}{\tau}_{ij}$ is the Oldroyd upper convected derivative:

204
$$\overset{\nabla}{\tau}_{ij} = \frac{\partial \tau_{ij}}{\partial t} + \frac{\partial}{\partial x_k} (\mathbf{u}_k \tau_{ij}) - \left(\tau_{ik} \frac{\partial \mathbf{u}_j}{\partial x_k} + \tau_{kj} \frac{\partial \mathbf{u}_i}{\partial x_k} \right) \quad (10)$$

205 The viscoelastic stress tensor has 9 components, however since the matrix is
 206 symmetric, 6 transport equations are solved to get the full solution for τ_{11} , $\tau_{12} = \tau_{21}$,
 207 $\tau_{13} = \tau_{31}$, τ_{22} , $\tau_{23} = \tau_{32}$ and τ_{33} . At the end of each iteration, the values of the
 208 velocity gradient tensor are used to calculate the viscoelastic stress terms. The
 209 viscoelastic stress source term (equation (3)) is then added to the momentum
 210 equations in the subsequent iteration. Subgrid scale viscoelastic effects are neglected
 211 in calculations since, to the best of our knowledge, no such models have been
 212 developed for PTT fluids as this requires direct numerical simulation and experimental
 213 data for validation.

214 A pressure based solver is employed to solve the differential equations using the
 215 commercial code Fluent 17.0 with user defined functions for implementation of the
 216 viscoelastic model and the results are post processed using the Tecplot software.

217 Temporal integration is performed using second order implicit backward discretization.
 218 Momentum equations are solved using gamma differencing scheme⁸¹ and viscoelastic
 219 stress terms are discretized with first order upwind scheme. Moreover, an artificial
 220 diffusion term is added to the viscoelastic stress transport equations, such that the
 221 dimensionless artificial diffusivity ($D = k/u\tau H$, where k is constant artificial diffusivity,
 222 $u\tau$ is the friction velocity and H is the nozzle width) is kept below 0.1, this was
 223 necessary in order to achieve a stable solution by smoothing the sharp gradients in the
 224 viscoelastic stress terms⁸². The vapor volume fraction transport equation is discretized
 225 with the quadratic upstream interpolation for convective kinetics (QUICK) scheme to
 226 achieve an accurate representation of the high density ratio field.

Table I. Boundary conditions at inlet and outlet surfaces. Total pressure values are taken from the injection pressure and downstream pressure values reported in Table II

Boundary value	Boundary condition
Inlet and outlet pressure	Dirichlet static pressure: $p_{\text{static}} = p_{\text{total}} - 0.5\rho u_i u_i$
Inlet normal velocity	Neumann: $\frac{\partial u_1}{\partial x_1} = 0$
Inlet tangential velocity	Dirichlet: $u_2 = u_3 = 0$
Inlet and outlet viscoelastic stresses	Neumann: $\frac{\partial \tau_{ij}}{\partial x_k} \mathbf{e}_i \otimes \mathbf{e}_j \otimes \mathbf{e}_k = 0$
Inlet vapor volume fraction	Dirichlet: $\alpha = 0$
Outlet velocity	Neumann: $\frac{\partial u_i}{\partial x_j} \mathbf{e}_i \otimes \mathbf{e}_j = 0$
Outlet vapor volume fraction	Neumann for $u_i n_i > 0$: $\frac{\partial \alpha}{\partial x_i} = 0$ Dirichlet for $u_i n_i < 0$: $\alpha = 0$ (n is the normal vector)

227

228 In the step nozzle test case, pressure and velocity are linked using the pressure implicit
 229 with splitting of operator (PISO) algorithm which is based on a predictor-corrector
 230 approach. Initially, the momentum equation is solved using a guessed pressure field. A

231 pressure correction equation which is derived from the momentum and continuity
 232 equations, is then used to correct the velocities⁸³.

233 In the injector test case, a coupled pressure based solver was used in order to achieve
 234 a faster convergence rate compared to the aforementioned segregated solver. In the
 235 coupled solver algorithm, the pressure and momentum are solved simultaneously and
 236 the pressure corrector is used to update the velocities⁸⁴.

Table II. Operating conditions for the step nozzle and the injector nozzle simulations. Cavitation number is calculated from equation (11)

Test case	Injection pressure P_{in} (KPa)	Downstream pressure $P_{downstream}$ (KPa)	Saturation pressure P_v (KPa)	Cavitation number Cn
Step nozzle	238.2	101.3	2.3	1.38
Injector	182385	5066.2	130	35.9

237

238 The polymer relaxation times chosen in this study (reported in Table III) are in the range
 239 measured for dilute viscoelastic solutions in low viscosity solvents⁸⁵. The molecular
 240 weight of the polymer used in the non-polar solution in the study are reported 6.9 g/mol
 241 and 1.6 g/mol for the polymer in the aqueous solution and the concentration range
 242 corresponding to the chosen relaxation times is $\sim 0.1\%$ wt. The relaxation times are
 243 large compared to the flow time scales such as the turnover time of large and small
 244 eddies so it is expected that they alter the flow topology. When polymer relaxation
 245 times are comparable to flow time scales, the turbulent kinetic energy cascade can be
 246 altered resulting in turbulent drag reduction^{49,86}.

247 To characterize the polymer viscosity, the viscosity ratio β is used ($\beta = \mu_s / \mu_0$), where

248 $\mu_0 = \mu_s + \mu_p$ is the total viscosity and μ_s and μ_p are the solvent and the polymer

249 viscosities. One of the main objectives of this study is to examine how viscoelasticity
 250 can affect the cavitation structures. For this purpose we conducted a preliminary study
 251 on the effect of the polymer viscosity and observed clear changes (instantaneous and
 252 time-averaged) in cavitation volume fraction when the viscosity of the polymer was
 253 large compared to the solvent viscosity. High polymer viscosity values (when β is as
 254 small as 0.2)⁸⁷ can damp the turbulent shear stress and contribute to reduction of the
 255 turbulent drag⁸⁷.

Table III. Fluid properties for the step nozzle and the injector nozzle simulations. *For Diesel liquid viscosity, the Kolev correlation in equation (14) is used, β value is then calculated from the average viscosity in the flow field.

Test case	Fluid	Liquid density ρ_l (Kg/m ³)	Vapor density ρ_v (Kg/m ³)	Liquid (solvent) viscosity μ_s (Pa.s)	Vapor viscosity μ_v (Pa.s)	Polymer viscosity μ_p (Pa.s)	Polymer relaxation time λ (s)
Step nozzle (Newtonian)	Water	998.16	1.71E-02	1.02E-03	9.75E-06	-	-
Step nozzle (Viscoelastic)	$\beta = 0.1$	998.16	1.71E-02	1.02E-03	9.75E-06	9E-03	4E-02
Injector (Newtonian)	Diesel	747.65	6.56	Eq 14	7.50E-06	-	-
Injector (Viscoelastic)	$\beta = 0.1^*$	747.65	6.56	Eq 14	7.50E-06	2E-02	8E-03

256

257

258 **2.1. Step nozzle test case**

259 The geometry of the step nozzle is shown in Figure 1(a) which is based on an
 260 experimental study⁸⁸ designed to investigate cavitation in a rectangular injector.
 261 Cavitation development inside the nozzle from incipient condition to fully developed
 262 condition is visualized using high speed imaging, moreover laser doppler velocimetry
 263 (LDV) measurements of streamwise velocity and RMS of turbulent velocity are
 264 provided for incipient cavitation condition in water. These experimental data were

265 previously used to examine the performance of the turbulence model and the cavitation
266 model used in the current study⁸⁹. The data is only available for water and to the best
267 of author's knowledge no studies in the literature provide similar data for viscoelastic
268 cavitating flows.

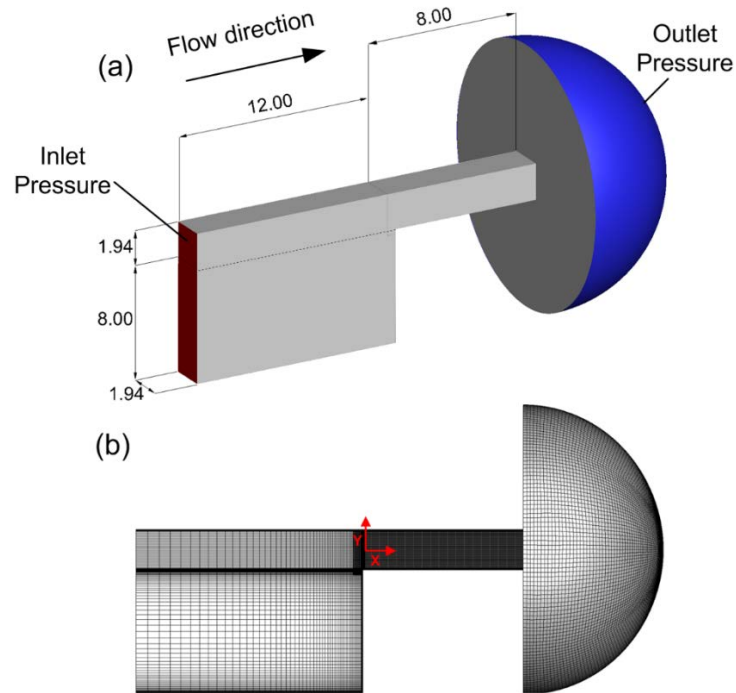
269 Cavitation starts to develop inside the nozzle as water is injected at 0.16 MPa into the
270 atmospheric pressure while the flowrate is 40 mL/s. The injection pressure is increased
271 and cavitation intensifies until fully developed cavitation conditions are reached at 0.31
272 MPa injection pressure and 62 mL/s flowrate.

273 A hemispherical outlet geometry is added to the domain with 14 mm diameter to allow
274 a uniform assignment of the outlet pressure boundary condition away from the nozzle
275 exit and boundary and operating conditions are reported in Table I and Table II.

276 In the simulation test case water flows through the nozzle with a flowrate of 48 mL/s,
277 the pressure difference across the nozzle is 1.38 bar while the injected liquid is
278 discharging into atmospheric pressure. The cavitation number (Cn defined in Equation
279 (11), $P_{\text{injection}}$, $P_{\text{downstream}}$ and P_v are the injection, downstream and vapor pressures
280 respectively) is 1.38 and the Reynolds number based on average liquid velocity in the
281 nozzle is 27700. These values are similar to those realized in real-size diesel injectors
282 operating at nominal injection pressures and correspond to the incipient cavitation
283 regime⁸⁸:

284

$$Cn = \frac{P_{\text{injection}} - P_{\text{downstream}}}{P_{\text{downstream}} - P_v} \quad (11)$$



285

286 *Figure 1. (a) Geometry of the step nozzle and the relevant dimensions in mm, inlet boundary*
 287 *(red color) and outlet boundary (blue color) surfaces are shown all the other surfaces are no-*
 288 *slip walls (grey color) (b)Computational grid with additional refinement inside the nozzle*

289 The computational grid consists of unstructured hexahedral cells and additional
 290 refinement is used inside the constriction to achieve the cell size below the Taylor
 291 length scale λ_g (approximated from the characteristic length scale $L = 1.94$ mm and
 292 Reynolds number, $\lambda_g = (10/Re)^{0.5} L = 39 \mu\text{m}$). Estimation of Taylor microscale provides
 293 a guideline for grid resolution in practical LES studies^{90,91}; by refining the mesh below
 294 this value the large scale turbulent eddies are captured as λ_g theoretically lies in the
 295 high wavenumber end of the inertial subrange. Taylor length scale characterizes the
 296 mean spatial extension of the velocity gradients^{92,93} and is always much smaller than
 297 the integral scale (but not the smallest scale)⁹⁴. The cell size inside the nozzle is $20 \mu\text{m}$
 298 and it is refined to $2.5 \mu\text{m}$ near the walls, corresponding to y^+ values of 0.2-1. The time
 299 step corresponding to Courant-Friedrichs-Lewy (CFL) number of 0.5 is set to $1 \mu\text{s}$ in
 300 the Newtonian test case and for the viscoelastic case the time step is reduced to $0.5 \mu\text{s}$
 301 for CFL of 0.25.

302 **2.2. Injector nozzle test case**

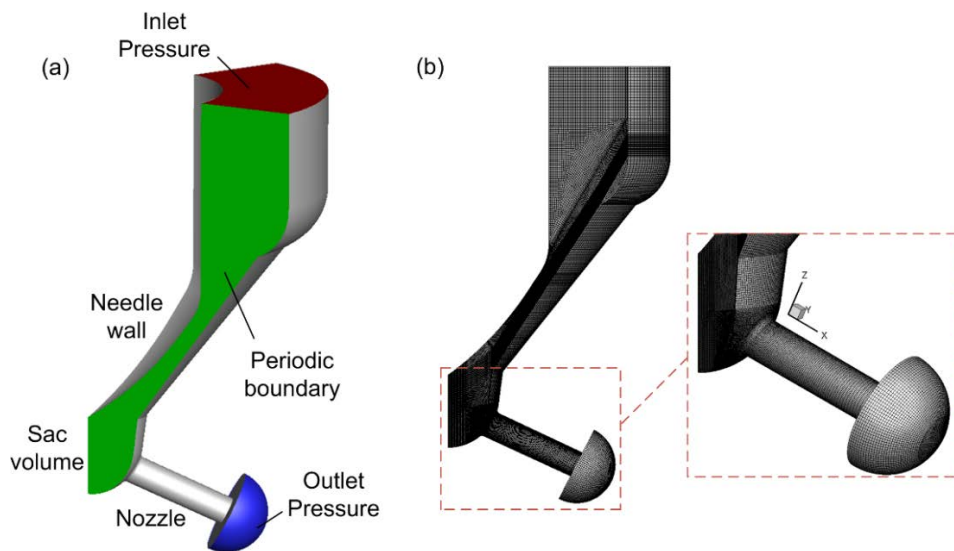
303 A common rail injector geometry section as shown in Figure 2 is simulated which has a
304 more complex flow and cavitation mechanism compared to the step nozzle. This is a
305 real-size Diesel fuel injector tip with five uniformly distributed holes and the nozzle
306 holes are slightly tapered with a k factor of 1.1:

$$307 \qquad k = \frac{D_{in} - D_{out}}{10} \qquad (12)$$

308 D_{in} and D_{out} are inlet and outlet diameters of the hole measured in micrometers. The
309 nozzle has an inlet and exit diameter of 0.37 mm and 0.359 mm respectively and is 1.26
310 mm long. Nozzle hole tapering is linked to reduction of cloud cavitation but at the same
311 time, formation of vortex or string cavities (presented in results section in Figure 10)
312 inside the nozzle. By using tapered holes instead of cylindrical holes, string cavitation
313 which forms inside large scale vortices entering the nozzle from the sac volume, can be
314 intensified while cloud cavitation is reduced⁷⁰. In this test case, the fuel passes through
315 the needle passage before entering the sac volume (see Figure 2), where it recirculates
316 as it enters the nozzle. A cavitation cloud forms at the top corner of the nozzle entrance
317 due to the sharp turn in the flow streamline. Moreover, a large vortex enters the nozzle
318 from the sac volume, with string cavitation forming in the core of this vortex inside the
319 nozzle. A recent fully compressible implicit LES simulation of a 9-hole injector with
320 needle motion⁹⁵ shows that elongated vortical structures which enter the nozzle from
321 the sac volume and the overall flow features are present when compared to steady
322 needle simulations at full needle lift.

323 The Reynolds number inside the nozzle and the sac volume reaches above 30,000
324 indicating the highly turbulent flow conditions of the injector. Considering the mesh
325 resolution and the small time step required for simulating this case, the computational

326 cost of simulating the complete 5 hole geometry for Newtonian and viscoelastic fluids
 327 would be very high so 1/5th of the injector geometry (72°) is simulated as shown in
 328 Figure 2 (b) and periodic boundary conditions are employed on the sides of the
 329 geometry.



330

331 *Figure 2. (a) Simulation domain for the injector test case. Boundary condition are indicated by*
 332 *colored surfaces; inlet and outlet boundaries are colored in red and blue respectively and the*
 333 *green surface shows the periodic boundary (another periodic boundary with the same cross*
 334 *section is located on the opposite side of the geometry), all the other surfaces are no-slip walls*
 335 *(grey color), (b) The computational grid for the injector, the domain is partitioned using blocking*
 336 *and it is hex-dominant except from an unstructured tetrahedral section in the sac volume*

337 Inlet and outlet total pressures are fixed at $P_{\text{injection}} = 1800$ bar and $P_{\text{downstreamt}} = 50$ bar.

338 Cavitation number for this condition is $Cn = 35.9$, which is much higher than the step
 339 nozzle test case due to the higher pressure difference from the inlet to the outlet. In this
 340 condition fully developed cloud cavitation is located in the top surface of the nozzle,
 341 while the string cavity has a more intermittent appearance.

342 A hex-dominant block mesh is used for most parts of the geometry, except for a section
 343 in the sac volume upstream of the nozzle entrance, where unstructured tetrahedral
 344 mesh is used. The mesh resolution in the nozzle and the sac volume where cavitation
 345 develops is $7.5 \mu\text{m}$ with additional refinement near the walls. With this resolution, large
 346 scale flow structures, unsteady cavitation dynamics and vortex shedding can be

347 captured. The time step for the Newtonian flow condition is 5 ns for CFL of ~0.4 and for
348 the viscoelastic case it is reduced to 2 ns and CFL of ~0.15.

349 The pressure levels inside the injector change significantly so the subsequent changes
350 in the Diesel fuel properties are also considered. Hence the density and the viscosity of
351 the fuel are calculated as a function of pressure. The density is calculated using Tait
352 equation of state to represent the weak compressibility of the liquid Diesel:

$$353 \quad p = B \left[\left(\frac{\rho}{\rho_{\text{sat,L}}} \right)^n - 1 \right] + P_{\text{sat}} \quad (13)$$

354 where the bulk modulus B is 110 MPa, the material exponent n is 7.15 and $\rho_{\text{sat,L}}$ and
355 P_{sat} are the liquid saturation density and saturation pressure respectively. The liquid
356 viscosity is calculated based on the correlation proposed by Kolev⁹⁶ :

$$357 \quad \log_{10} \left(\frac{10^6 \mu_L}{\rho} \right) = 0.035065275 - \frac{0.000234373 p}{10^5} \quad (14)$$

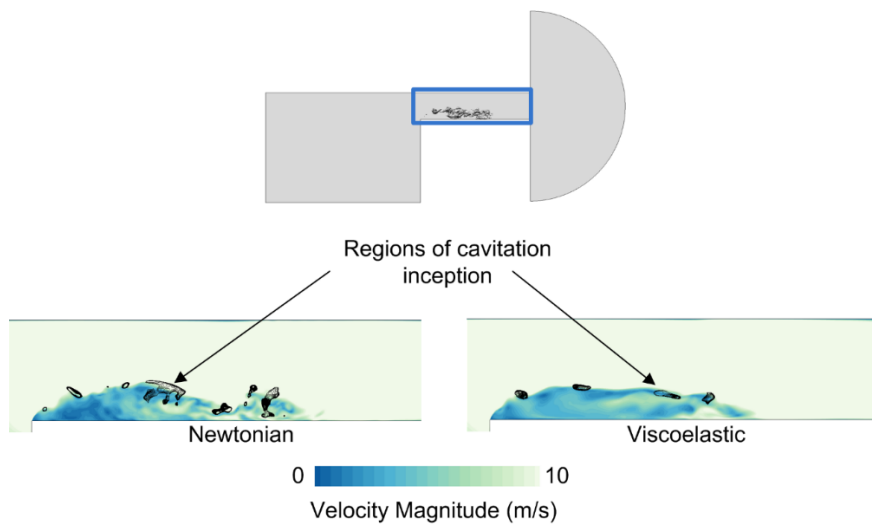
358 The values used for the fluid properties used in both test cases can be found in Table
359 III.

360 **3. Results and discussion**

361 **3.1. Step nozzle**

362 As the flow detaches at the entrance of the nozzle (see Figure 3) a shear layer is
363 formed between the flow passing through the nozzle and the recirculation region.
364 Cavitation vapors appear in the core of microvortices in the shear layer and they are
365 detaching and shedding from the cavity cloud in a cyclic manner. Contours of velocity
366 magnitude in the mid-plane of the nozzle for the Newtonian and the viscoelastic fluids
367 are presented in Figure 3. It is evident that the flowfield in the viscoelastic fluid appears

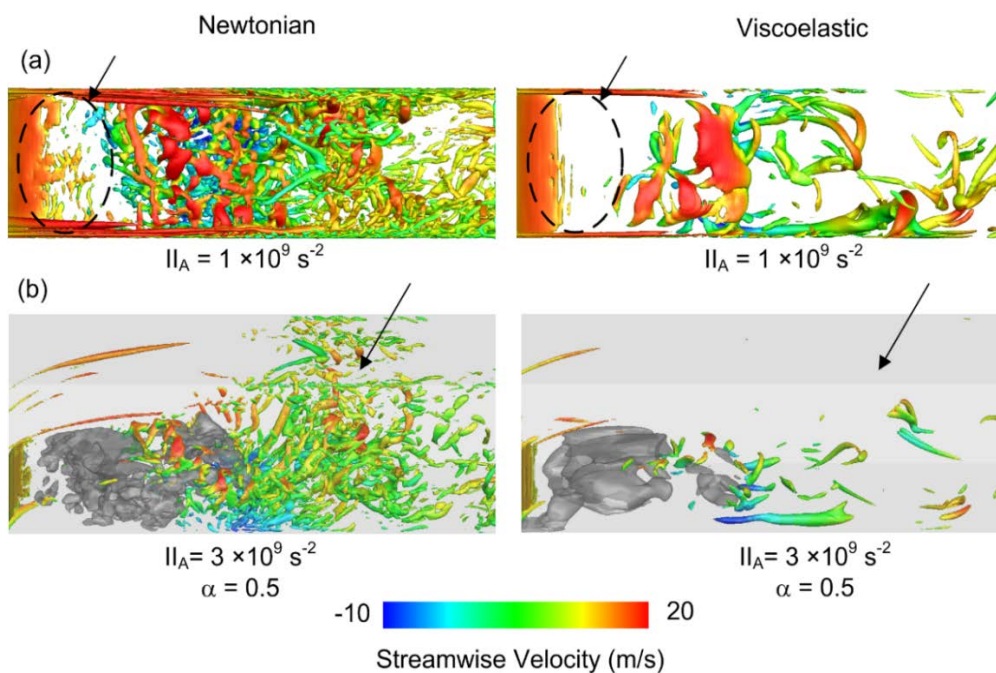
368 to have a more homogenous gradient. The black iso-lines show the areas where the
 369 pressure drops below the vapor pressure, i.e. the regions of cavitation inception. The
 370 cavitation inception regions appear more frequently in the Newtonian fluid and they
 371 cover a larger area of the nozzle's cross sectional area, indicating that more vapor is
 372 being produced in this fluid. It is likewise reported in the literature that the minimum
 373 pressure at a cavitation inception point (the core of a vortex developing in the wake of a
 374 cylinder) increases as the vorticity is reduced by viscoelasticity⁹⁷.



375
 376 *Figure 3. Nozzle geometry and cavitation in the shear layer (top), contours of the velocity*
 377 *magnitude for the Newtonian and the viscoelastic fluid in the mid-plane of the nozzle, the black*
 378 *iso-lines show regions with pressures below the vapor pressure (bottom)*

379 The structure of the vortical features in the flow is shown in Figure 4 by means of the
 380 second invariant of the velocity gradient tensor⁹⁸ calculated from $\Pi_A = -\frac{1}{2} \frac{\partial \mathbf{u}_i}{\partial x_j} \frac{\partial \mathbf{u}_j}{\partial x_i}$.
 381 Spanwise Kelvin-Helmholtz-like vortices form right after the nozzle inlet as shown in
 382 Figure 4 (a), it can be clearly seen that significantly fewer vortices appear in the
 383 viscoelastic fluid. Inhibition of shear instability by polymer injection has previously been
 384 reported in the literature⁹⁹. The ‘polymer torque’, which is the contribution of the
 385 viscoelastic stress to the vorticity evolution, increases the flow resistance to rotational
 386 motion and can inhibit the vortex sheet roll-up⁹⁷.

387 Further downstream, the vortex sheet breaks down, developing a range of small-scale
 388 and large-scale structures. It is evident that in the viscoelastic fluid spanwise vortices
 389 are inhibited while longitudinal vortices become more dominant. Enhancement of large
 390 scale coherent structures in the mixing layer is due to hindering of development of
 391 perturbations and a stronger vorticity diffusion in viscoelastic fluids¹⁰⁰. This results in
 392 slower rotational motion of the neighboring vortices and delay of vortex pairing and
 393 merging, therefore the lifetime and the scale of the coherent structures is increased.



394

395 *Figure 4. (a) Iso-surface of the second invariant of the velocity gradient with the value $1 \times 10^9 \text{ s}^{-2}$*
 396 *colored with the streamwise velocity, image shown from the top ($-Y$) direction (b) 3D view of the*
 397 *iso-surface of the second invariant of the velocity gradient at $3 \times 10^9 \text{ s}^{-2}$ colored with the*
 398 *streamwise velocity along with iso-surface of 50% vapor volume fraction (grey color)*

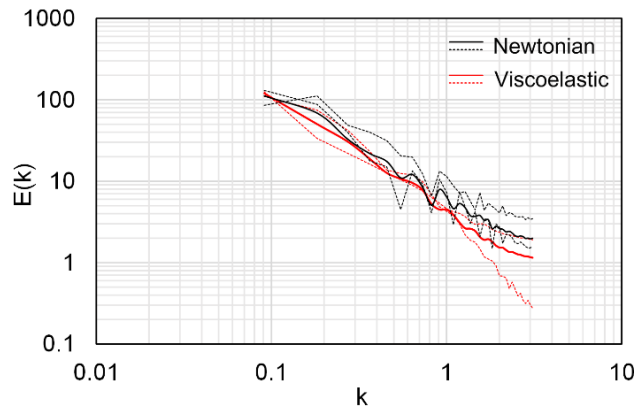
399 In Figure 4 (b) the iso-surface of 50% vapor volume fraction is presented along with the
 400 II_A iso-surface. After the collapse of the cavity cloud in the Newtonian fluid, a strong
 401 mixing region forms inside the nozzle. In the viscoelastic fluid however, the mixing is
 402 weaker and mainly vortices with larger diameters are forming as local instabilities are
 403 suppressed and vortical sub-structures are damped. Likewise enlargement of
 404 streamwise vortical structures and their elongation in the streamwise direction is

405 reported in turbulent channel flows¹⁰¹. This is due to tendency of polymers to strongly
406 align in the streamwise direction, partially suppressing wall-normal and spanwise
407 velocity fluctuations¹⁰². Moreover, the polymer viscosity resists the extensional
408 deformation imposed by the motion of turbulent eddies^{103,104}.

409 The turbulence kinetic energy spectrum for the Newtonian and the viscoelastic fluid is
410 shown in *Figure 5*, where k is the wave number and $E(k)$ is the amplitude of the kinetic
411 energy FFT calculated inside the nozzle. The graph represents the spatial spectrum of
412 the turbulence kinetic energy, where $k = 2\pi n/L$ and n and L are the incremental spatial
413 frequency number and the wavelength respectively.

414 Energy content of the low wavenumber scales is higher by ~15% in the Newtonian
415 fluid, however the decay slope is also slightly faster (-5/3 in the Newtonian fluid in
416 competition with ~-4/3 in the viscoelastic fluid) so the flow energy mainly contained
417 within the inertial subrange eddies is similar in both cases.

418 At higher wavenumbers the difference becomes more evident as the Newtonian fluid
419 has ~38% higher turbulence kinetic energy content, indicating that the small-scales in
420 this fluid are more pronounced. This observation is expected as the small-scales are
421 suppressed in the viscoelastic fluid as seen in *Figure 4*. This is consistent with
422 experimental measurements of power spectra in wall-bounded polymeric flows which
423 show that viscoelasticity can suppress turbulence kinetic energy at small-scales while
424 having a negligible effect on large scales¹⁰⁵. Moreover, in viscoelastic fluids, the kinetic
425 energy removed from the large scales is partially dissipated by small-scales and
426 partially converted into elastic energy which is then transferred back into the large
427 scales. This will alter the nature of energy cascade usually seen in Newtonian fluids
428 and reduce the energy content at the small-scales¹⁰⁶.



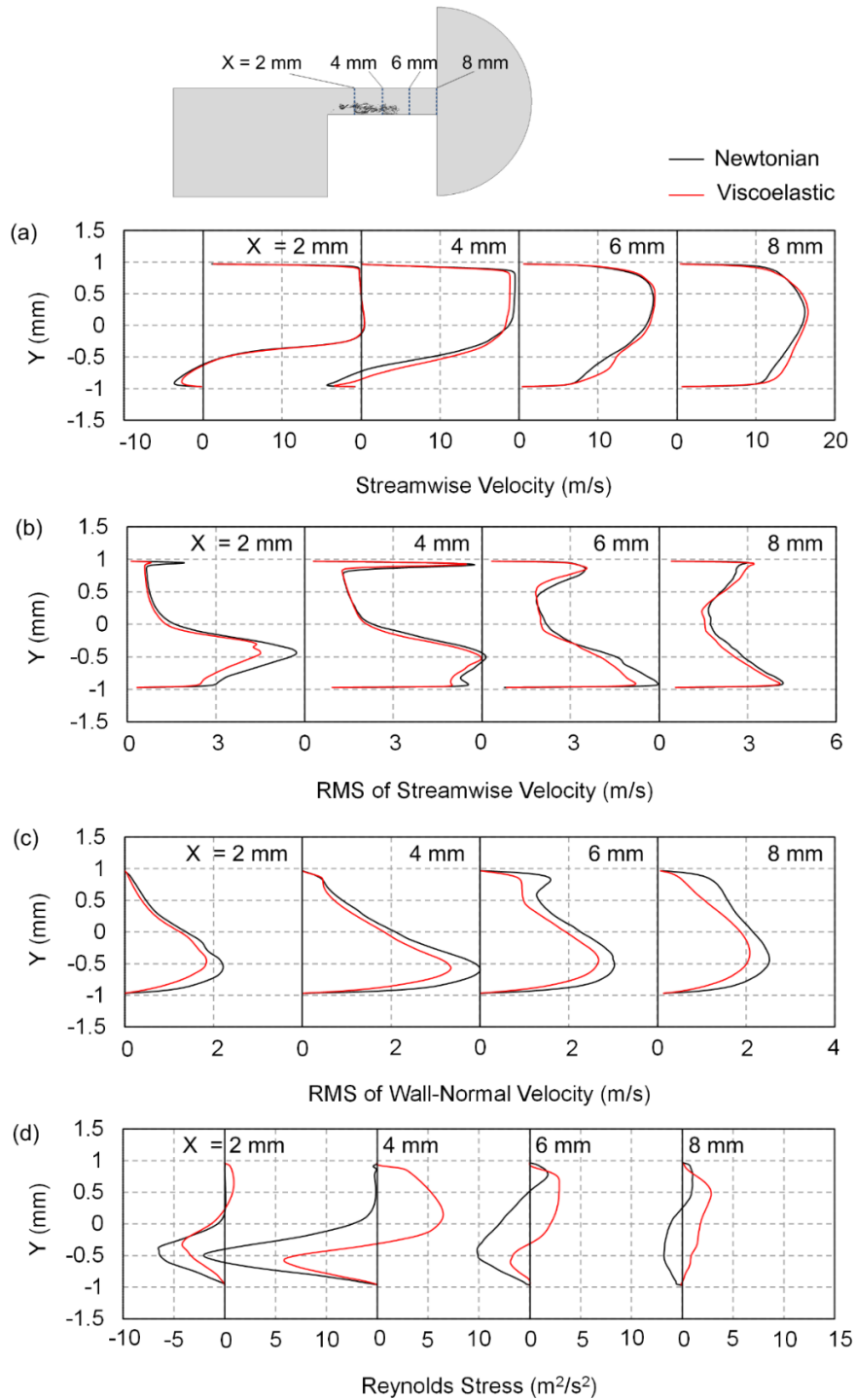
429

430 *Figure 5. Energy spectra inside the step nozzle for the Newtonian and the viscoelastic fluid,*
 431 *dashed lines (..... and)* show indicative examples of the spectra and continuous lines (—
 432 *and —)* show the mean value of the spectra for the Newtonian and viscoelastic fluid

433 In *Figure 6 (a)* the development of the streamwise velocity component in the mid-plane
 434 of the nozzle presented. The magnitude of the negative velocity in the recirculation
 435 region ($-0.94 \leq Y \leq -0.4$) is larger in the Newtonian fluid on average by ~28% at $X =$
 436 2mm and ~41% at $X = 4$ mm. The re-entrant jet velocity is responsible for detachment
 437 and shedding of the cavity cloud ⁷¹, therefore larger velocities in the recirculation region
 438 of the Newtonian fluid are indicative of a faster shedding process in this fluid.

439 In *Figure 6 (b)*, the RMS of streamwise velocity which indicates the turbulent velocity, is
 440 plotted along the nozzle. Overall the weighted average of RMS of streamwise velocity
 441 over the computational cell volume inside the nozzle ($0 \text{ mm} < X < 8 \text{ mm}$) is reduced by
 442 11% in the viscoelastic fluid. In *Figure 6 (b)*, this effect is mainly visible in the lower half
 443 of the nozzle ($-0.94 \text{ mm} \leq Y \leq 0 \text{ mm}$), corresponding to the shear layer and flow
 444 recirculation regions. The effect of viscoelasticity on velocity fluctuations is more
 445 evident in *Figure 6 (c)* which shows the RMS of wall-normal velocity along the nozzle.
 446 Suppression of velocity fluctuations is stronger in the wall-normal direction compared to
 447 the streamwise direction and overall the RMS of wall-normal velocity is reduced by
 448 27.5% inside the nozzle for the viscoelastic fluid. By suppressing the wall-normal

449 velocity fluctuations, polymers can more effectively reduce the turbulence generation
 450 by vortices.



451

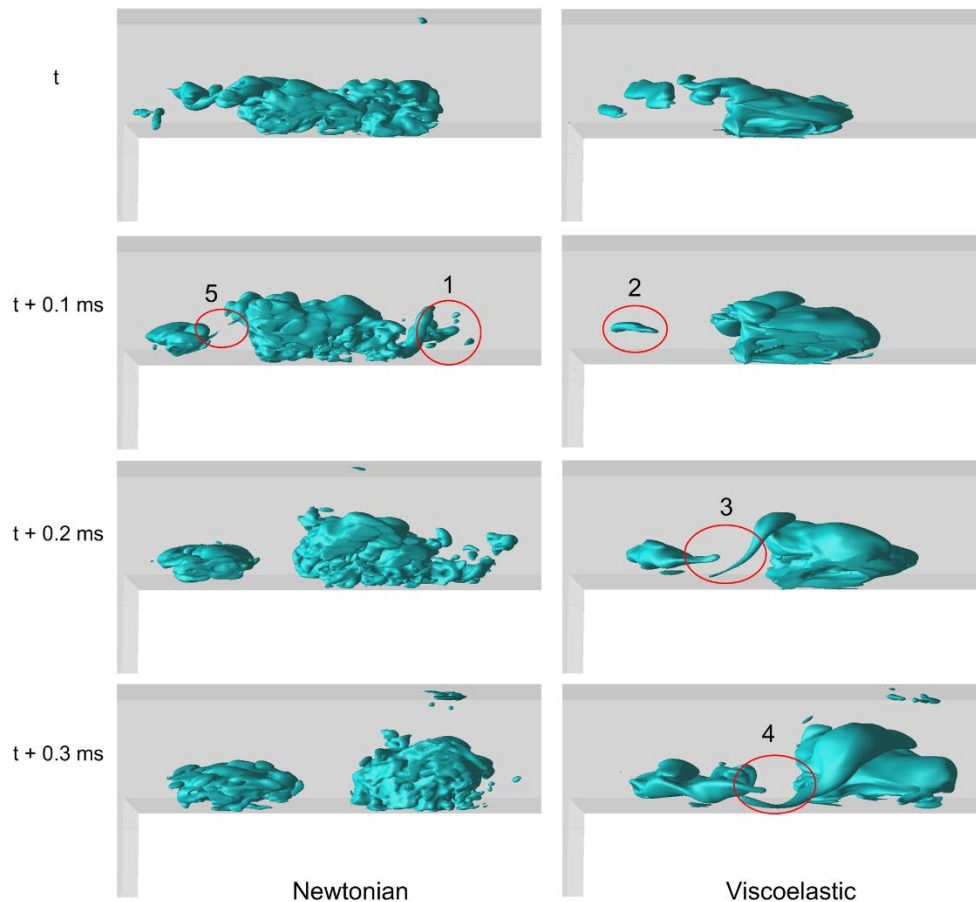
452 *Figure 6. Comparison of time-averaged values of the streamwise velocity, RMS of streamwise*
 453 *velocity, RMS of wall-normal velocity and Reynolds stress ($-\overline{u'v'}$) in the Newtonian and the*
 454 *viscoelastic fluid, data are presented in the mid-plane of the step nozzle at four different X*
 455 *locations along the nozzle*

456 In Figure 6 (d) the Reynolds stress in the XY plane ($-\overline{u'v'}$) is plotted along the nozzle,
457 positive and negative values of the Reynolds stress correspond to turbulence
458 suppression and production respectively¹⁰⁷. Negative values of Reynolds stress are
459 produced by ejection and sweep motions which contribute to positive turbulence
460 production and in general increase drag. Positive Reynolds stress values correspond to
461 turbulence suppression and their increase generally results in drag reduction ¹⁰⁷. It is
462 evident that in the recirculation region ($-0.94 \text{ mm} \leq Y \leq 0 \text{ mm}$) the Newtonian fluid has
463 about twice the amount of Reynolds stress generated in the viscoelastic fluid, resulting
464 in a higher level of turbulence generated in this region. In the bulk of the flow outside
465 the recirculation zone, Reynold stresses have a positive value with a higher magnitude
466 in the viscoelastic fluid indicating a stronger turbulence damping. Overall, stronger
467 turbulence damping and lower turbulence levels generated in the viscoelastic fluid as
468 seen in Figure 6 (b)-(d), can contribute to turbulence drag reduction and the mass
469 flowrate is increased by~2%.

470 In *Figure 7* the development of cavitation inside the nozzle for the Newtonian and the
471 viscoelastic fluid is compared in terms of 25% vapor volume fraction iso-surface.
472 Cavitation is initiated in the core of microvortices forming in the shear layer and it grows
473 as larger eddies form after the vortex sheet breakdown. Following, they form a cavity
474 cloud which detaches due to the re-entrant jet motion and is convected toward the
475 nozzle exit.

476 In the Newtonian fluid, small cavitation structures can be observed (red circle 1) with
477 microcavities of various sizes (approximate diameter range of $30 \mu\text{m}$ - $200 \mu\text{m}$) shedding
478 from the cloud, however such structures are not present in the viscoelastic fluid.

479



480

481 *Figure 7. Cavitation development inside the step nozzle presented by means of 25% vapor*
 482 *volume fraction iso-surfaces, data are presented every 0.1 ms. Small microcavities shedding*
 483 *from the cloud (red circle 1) are not present in the viscoelastic fluid, cavitation vapors can*
 484 *initially shrink before growing (red circle 2) and larger streamwise vortices appear between the*
 485 *detached cloud and shear layer cavitation structures (red circle 3, 4 and 5)*

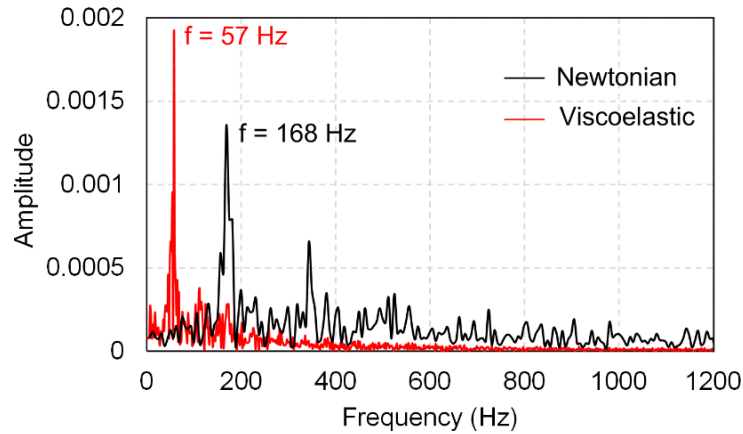
486 The growth of the shear layer cavitating microvortices is rather faster in the Newtonian
 487 fluid; in the viscoelastic fluid it appears that the cavity initially shrinks (red circle 2)
 488 before growing. This can be due to the action of viscoelastic force resisting the fast
 489 deformation by liquid evaporation. Furthermore, cavitation structures in the viscoelastic
 490 fluid have an elongated shape. Larger streamwise cavitating vortices appear between
 491 the shear layer cavities and the detached cloud compared to the Newtonian fluid (see
 492 red circles 3, 4 and 5).

493 Due to the cyclic enlargement and shrinkage of the flow recirculation zone and the
 494 subsequent detachment and shedding of the cavitation vapors, the mass flowrate in the

495 nozzle also fluctuates in a cyclic manner. The fast Fourier transform (FFT) of mass flow
496 rate time-evolution at nozzle outlet are presented in Figure 8 to indicate the dominant
497 frequencies of the mass flowrate fluctuations. The dominant frequency in the
498 Newtonian fluid is $f = 168$ Hz whereas in the viscoelastic fluid this value is reduced to f
499 $= 57$ Hz, while the peak amplitude is increased by 42%. First and second harmonics of
500 the dominant frequency can also be identified for both fluids at $\sim 2f$ (343 Hz for the
501 Newtonian fluid and 110 Hz for the viscoelastic fluid) and $\sim 3f$ (524 Hz for the
502 Newtonian fluid and 169 Hz for the viscoelastic fluid). Second harmonics with about
503 double the dominant frequency are reported in pressure signals past a cavitating
504 converging-diverging nozzle¹⁰⁸ and in the wake of a rectangular cavitating obstacle¹⁰⁹.

505 The reduction of the cavity shedding frequency can be due to the resistance of the
506 viscoelastic fluid to development of vortical structures and therefore suppression of
507 cavity growth in the core of vortices. Moreover, development of the cavitation cloud can
508 be delayed as the cavity volume can shrink before growing in the viscoelastic fluid due
509 to memory effects produced by fluid elasticity. In fact it was observed that some of the
510 shedding events are completely suppressed while vapor builds-up in the cloud region.
511 Therefore the subsequent shedding event is more violent in the viscoelastic fluid, thus
512 while the dominant frequency is reduced its peak amplitude is higher.

513 Unlike the Newtonian fluid, at frequencies above ~ 400 Hz there are effectively no
514 fluctuations in the viscoelastic fluid, indicating that the viscoelastic fluid damps out the
515 high frequency fluctuations. As the small-scale microcavities shedding from the
516 cavitation cloud are suppressed (Figure 7), the subsequent velocity fluctuations due to
517 growth, collapse and oscillations of these cavities can also be inhibited, resulting in
518 damping of high frequency fluctuations.



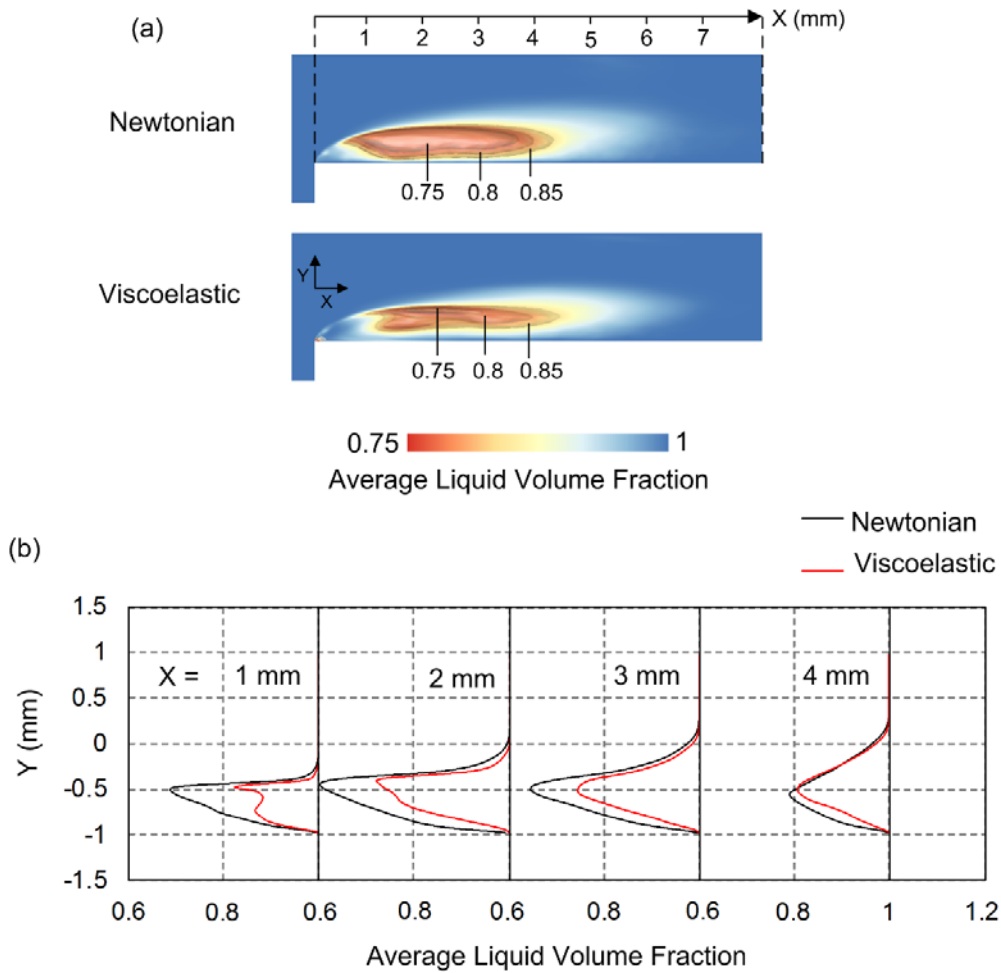
519

520 *Figure 8. FFT of mass flowrate fluctuations at the outlet of the step nozzle for the Newtonian*
 521 *and the viscoelastic fluid, the dominant frequency corresponds to frequency of mass flowrate*
 522 *fluctuations induced by cyclic growth and shedding of large cavity clouds*

523 The Strouhal number for vapor cloud shedding (St_v) based on the mass flowrate
 524 fluctuation frequency (f), the cavity length (L_v) and the average streamwise velocity in
 525 the cavity region (U_v) is defined as:

526
$$St_v = \frac{fL_v}{U_v} \quad (15)$$

527 For the Newtonian case the Strouhal number based on the dominant frequency is 0.22
 528 and in the viscoelastic fluid the Strouhal number is reduced to 0.08. For Newtonian
 529 fluids, a characteristic Strouhal number of 0.2 has been identified for cavitation cloud
 530 shedding in a diverging step⁷¹. The detachment and shedding of the cavitation cloud is
 531 partially driven by the re-entrant jet mechanism and the Strouhal number is
 532 proportional to the re-entrant jet velocity⁷¹, hence longer shedding periods can be due
 533 to reduction of the re-entrant jet velocity. Observations regarding the reduction of
 534 Strouhal number by viscoelasticity due to prolonged oscillation times has been reported
 535 for vortex shedding past an obstacle^{110–112}.



536

537 *Figure 9. (a) Average liquid volume fraction ($1-\alpha$) in the step nozzle mid-plane along with iso-*
 538 *surfaces of 75%, 80% and 85% average liquid volume fraction in the Newtonian and the*
 539 *viscoelastic fluid, (b) Average liquid volume fraction ($1-\alpha$) inside the cavitation region for the*
 540 *Newtonian and the viscoelastic fluid, values taken along 4 lines passing through the cavitation*
 541 *cloud in the nozzle mid-plane*

542 Finally, the time-averaged effect of viscoelasticity on the cavitation field is presented in
 543 Figure 9 by comparing the average liquid volume fraction inside the nozzle. It can be
 544 seen from Figure 9 (a) that the cavitation inception point is shifted further downstream
 545 the nozzle entrance; so vapor mainly starts to form at $X \approx 0.3$ mm in the Newtonian
 546 fluid and at $X \approx 0.8$ mm in the viscoelastic fluid. Moreover the thickness of the cavity
 547 cloud in this region is reduced from ~ 0.69 mm in the Newtonian fluid to ~ 0.58 mm in
 548 the viscoelastic fluid ($\sim 16\%$ reduction).

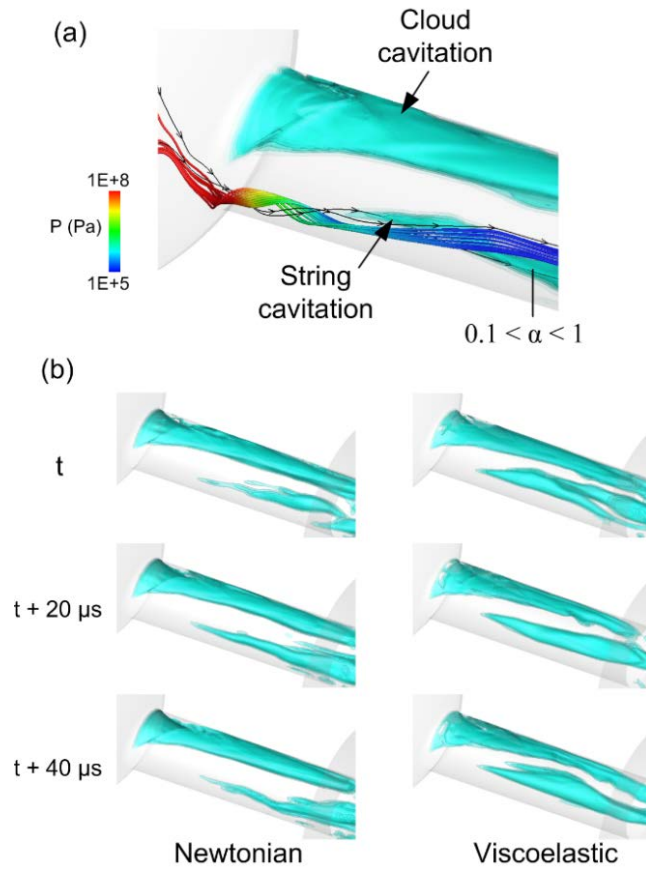
549 In Figure 9 (b) values of the liquid volume fraction in four locations inside the cavitation
550 cloud are compared. In all these locations the liquid volume fraction in the viscoelastic
551 fluid is constantly higher. The average vapor volume fraction in the viscoelastic fluid
552 integrated over the volume of the nozzle ($0 \text{ mm} < X < 8 \text{ mm}$) is reduced by 51%.
553 Moreover it is evident that the cavitation suppression effect is stronger at the lower half
554 of the cavity cloud $-0.94 \text{ mm} \leq Y \leq -0.5 \text{ mm}$ (closer to the nozzle wall). Reduction of
555 near wall vorticity fluctuations inhibits the near-wall eddies in viscoelastic fluids¹¹³ which
556 can be responsible for production and transport of cavitation vapors in this region.

557

558 **3.2. Injector nozzle**

559 In the injector nozzle, two distinct regions for cloud cavitation and string cavitation can
560 be identified. Characteristics of different cavitation mechanisms in injector nozzles is
561 described in the literature^{70,114,115}. The cloud cavitation forms in a similar manner to the
562 cavitation in the step nozzle; as the fluid enters the nozzle it takes a sharp turn at the
563 entrance forming a fully developed vapor cloud which is mainly attached to the top
564 surface of the nozzle and grows and sheds in a cyclic manner. The string cavitation
565 forms in the high vorticity core of a large vortex entering the nozzle from the sac
566 volume and it is located in the vicinity of the nozzle center (the streamlines and vectors
567 forming the string cavitation are presented in Figure 10 (a)).

568 The local pressure drops from 100 MPa in the sac volume to 0.1 MPa (below the
569 saturation pressure) inside the nozzle as the string cavity starts to form. The string
570 cavity has an intermittent appearance as it can distort, break-up and elongate inside
571 the nozzle, however in the viscoelastic fluid a larger and more stable vaporous core
572 appears and time averaged values of vapor volume fraction will be used to further
573 investigate this matter.



575

576 *Figure 10. (a) Two distinct cavitation regions forming inside the injector nozzle, cavitation*
 577 *vapors are presented using 5 translucent vapor volume fraction iso-surfaces ranging from 0.1 to*
 578 *1, the cavitating vortex can be seen entering the nozzle from the sac volume, the vortex is*
 579 *presented by streamlines colored with pressure (b) Indicative cavitation structures inside the*
 580 *nozzle at 20 μ s intervals for the Newtonian and the viscoelastic fluid ($0.1 < \alpha < 1$) showing a*
 581 *larger string cavity in the viscoelastic fluid.*

582 Since the cloud cavitation and the string cavitation occur at different locations inside
 583 the nozzle, it is possible to examine the effect of viscoelasticity on each cavitation
 584 mechanism by geometrically separating the cavitation vapor volumes as seen in Figure
 585 11 (a), which shows the separated cloud and the string cavitation structures in the
 586 same time step. The time-averaged vapor volume fraction data are separated into a
 587 cloud region and a string region by splitting the cross section of the nozzle into a top
 588 section (cloud, $Y > 35 \mu\text{m}$) and a bottom section (string, $Y < 35 \mu\text{m}$) using a plane along
 589 the nozzle axis. The vapor volume fraction in the string and the cloud region is

590 calculated in slices along the nozzle and the area weighted average value is used to
591 get the total vapor volume fraction. Vapor structures in the cloud and the string region
592 marginally intersect inside the nozzle but in the vicinity of the nozzle exit this overlap
593 can contribute to ~20% variations in the average vapor volume fraction in each region.
594 The overlapping regions are identified to be located in the area approximately $\pm 40\mu\text{m}$
595 from the nozzle axis and are displayed in the graph as error bars.

596 The time-averaged value of the total vapor volume fraction inside the nozzle is plotted
597 for the Newtonian and the viscoelastic fluid in Figure 11 (b). It is evident that the in-
598 nozzle cavitation mechanism is mainly due to cloud cavitation in the Newtonian fluid
599 and overall the vapor volume fraction in the Newtonian fluid is higher by 44%. Initially,
600 cavitation develops at the nozzle entrance due to the cloud cavitation mechanism,
601 increasing the vapor volume fraction in the nozzle up to ~0.16 in the Newtonian fluid
602 and up to ~0.08 in the viscoelastic fluid until $X \approx 0.4$ mm. After this point cloud
603 cavitation declines and string cavitation starts to develop while reaching the nozzle exit.
604 In the viscoelastic fluid the vapor volume fraction of the cloud cavitation is higher than
605 string cavitation up to $X \approx 0.9$ mm (70% into the nozzle length), and after this location
606 the string cavitation becomes more dominant. In the Newtonian fluid the rate of
607 reduction of the cloud cavity is ~17% faster than the rate of formation of string cavity,
608 hence the total vapor volume fraction is reduced after $X \approx 0.4$ mm. Whereas in the
609 viscoelastic fluid, the string cavitation forms more abruptly at a rate ~46% faster than
610 the decline of the cloud cavity, hence the total vapor volume fraction increases steadily
611 up to $X \approx 1$ mm, after this point vapor volume fraction is reduced as string cavitation
612 growth declines.

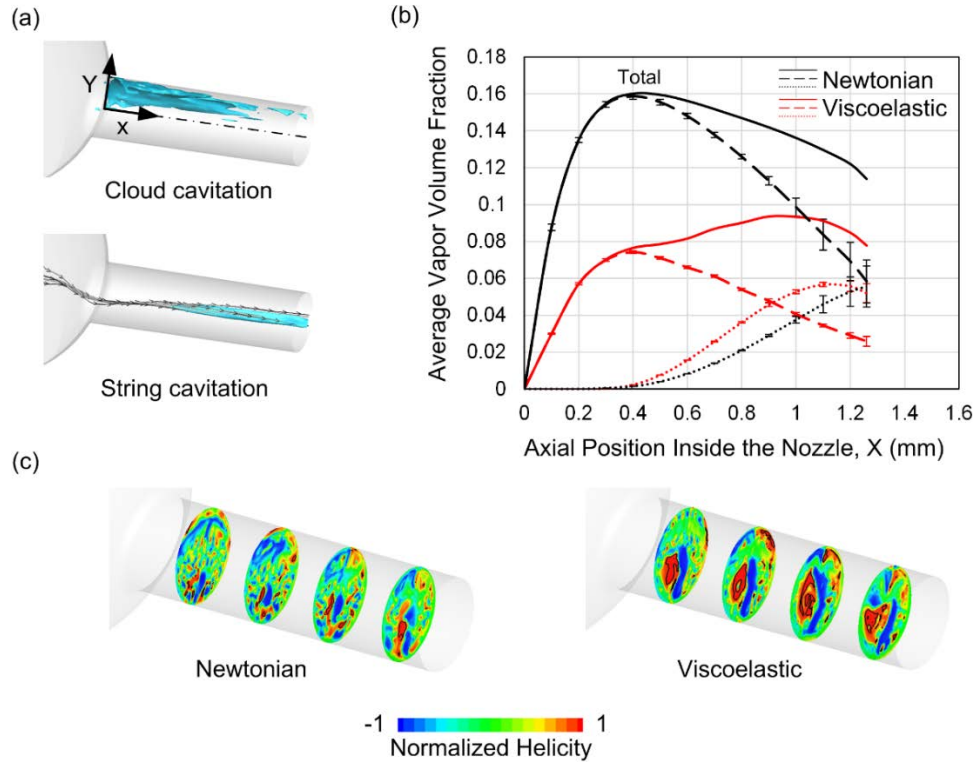
613 The main observation from comparing the changes in the vapor volume fraction in
614 different mechanisms is that viscoelasticity reduces cavitation formation in the cloud
615 cavitation region while increasing the string cavitation. This indicates that the strength

616 of the cavitating vortex in the nozzle core is increased in the viscoelastic fluid which
617 can be related to the alignment of the cavitating vortex with respect to the main flow
618 direction. The string cavitation is forming in the core of the quasi-streamwise vortex in
619 the center of the nozzle, whereas the cloud cavitation vortices can have large radial
620 velocity components which are expected to be inhibited by viscoelasticity.

621 In the core of vortices the angle between the velocity vector (U) and the vorticity vector
622 (ω) tends to zero as the vectors become aligned, hence the normalized helicity (H_n),
623 which is effectively the cosine of this angle, tends towards unity ¹¹⁶:

$$624 \quad H_n = \frac{U \cdot \omega}{|U||\omega|} \quad (16)$$

625 The normalized helicity contours are plotted in Figure 11(c) in several locations inside
626 the nozzle along with black isolines of $H_n = 0.95$. It is evident that in the viscoelastic
627 fluid, the string cavitation core covers a larger area, whereas in the Newtonian fluid a
628 smaller vortex core can be identified. In the step nozzle test case presented in the
629 previous section, it is reported that the streamwise vortices become more dominant by
630 viscoelasticity as the smaller scale vortices are damped. In wall-bounded viscoelastic
631 flows^{117,118} it is reported that streamwise vortices can become elongated and larger as
632 wall-normal fluctuations are damped. It is argued that suppression of cross-stream
633 fluctuations can further inhibit their auto-generation and therefore increase the lifetime
634 and strength of the longitudinal vortices. Likewise in this case, suppression of small-
635 scale eddies inside the injector nozzle can be responsible for stabilizing the local
636 turbulence in the vicinity of the string cavity, allowing the development of a larger
637 streamwise vortex and delaying the vortex breakdown, which in turn can result in
638 higher amounts of vapor to be produced in the vortex core.



639

640 *Figure 11. (a) Separated vapor volume fraction regions inside the injector nozzle showing the*
 641 *cloud cavitation and the string cavitation in term of iso-surfaces of 80% vapor volume fraction,*
 642 *(b) Development of the string cavitation (dotted lines..... and), the cloud cavitation (dashed*
 643 *lines --- and ---) and the total vapor volume fraction (continuous lines — and —) inside the*
 644 *injector nozzle for the Newtonian and the viscoelastic fluid calculated in slices along the nozzle*
 645 *axis using area weighted averages, error bars indicate the overlap of the vapor volume fraction*
 646 *in the string and cloud the region in $\pm 40\mu\text{m}$ in the vicinity of the nozzle axis, (c) Normalized*
 647 *helicity (H_n) contours in slices inside the injector nozzle (at $X = 0.2 \text{ mm}, 0.5 \text{ mm}, 0.8 \text{ mm}$ and 1.1*
 648 *mm), the black isolines show the regions of $H_n = 0.95$ and $H_n \rightarrow 1$ in vortex cores*

649 In the cavitation model of Schnerr and Sauer⁷⁸ in equation (7), the vapor volume
 650 fraction equation source term describes the mass transfer rate (R) between the two
 651 phases, so the positive values of R represent the evaporation rate and the negative
 652 values are the condensation rate:

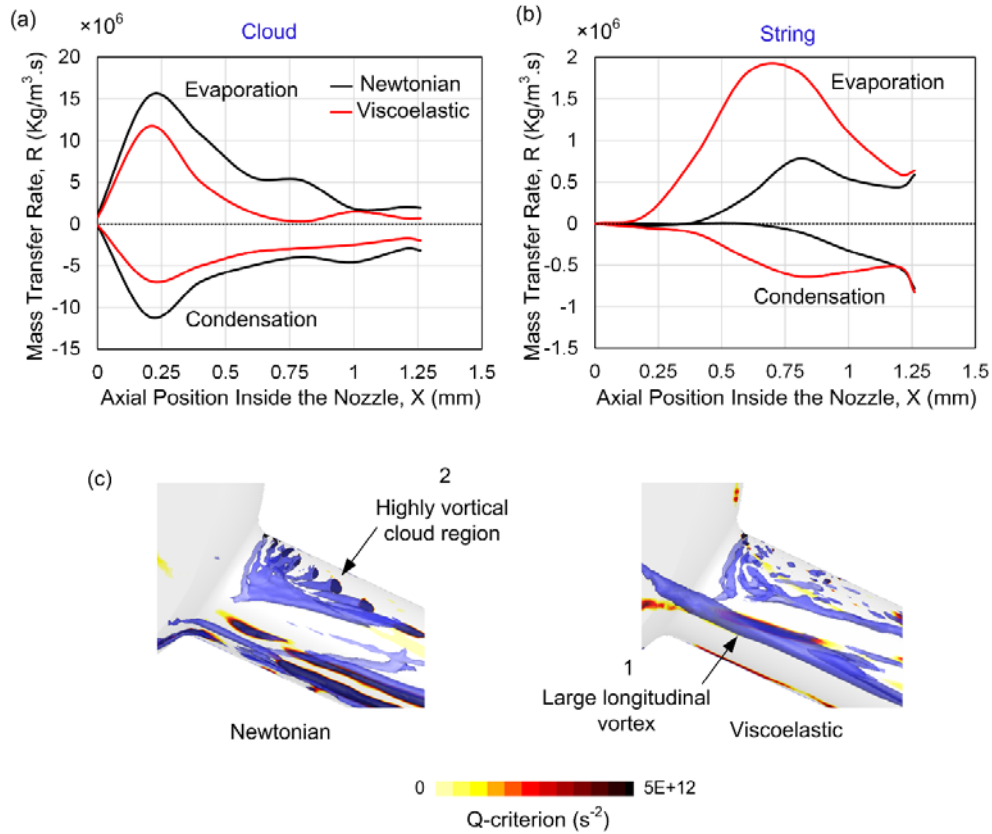
653

$$R = \frac{\rho_v \rho_l}{\rho_m} \alpha (1 - \alpha) \frac{3}{\Re_B} \left(\sqrt{\frac{2 |p_v - p|}{3 \rho_l}} \right) \text{sign}(p_v - p) \quad (17)$$

654 In Figure 12 (a) and (b) the phase change rates in the cloud cavitation and the string
 655 cavitation region at one instance are compared. The mass transfer rates are higher in
 656 the cloud cavitation region, reaching $15 \times 10^6 \text{ Kg/m}^3 \cdot \text{s}$ as opposed to $0.5 \times 10^6 \text{ Kg/m}^3 \cdot \text{s}$

657 in the string region of the Newtonian fluid, subsequently cloud cavitation is the main
658 mechanism of vapor production as it was seen in Figure 11 (b). In the cloud cavitation
659 graph, mass transfer starts at the $X = 0$ mm as the fluid enters the nozzle and peaks at
660 $X \approx 0.25$ mm, however the string cavitation starts effectively at $X > 0.2$ mm in the
661 viscoelastic fluid and $X > 0.4$ mm in the Newtonian fluid. The evaporation and
662 condensation rates in the cloud region are reduced in the viscoelastic fluid by ~ 2 orders
663 of magnitude, resulting in reduction of the vapor volume fraction in this region. However
664 in the string cavitation region this trend is reversed, i.e. evaporation rate is ~ 9 times
665 higher and condensation rate is ~ 2.5 times higher in the viscoelastic fluid.

666 The difference in the effect of viscoelasticity on cloud and string cavitation regimes can
667 be linked to the alignment of the vortical structures in each region with respect to the
668 direction of the main flow. The vortex cores identified in terms of the second invariant of
669 the velocity gradient are presented in Figure 12 (c). It is evident that viscoelasticity
670 does not affect the cloud and string vortical structures in the same manner. The vortex
671 which forms the string cavitation in the vicinity of the nozzle center (see arrow 1), is
672 enlarged by viscoelasticity while the vortical structures formed at the nozzle entrance in
673 the cloud region (see arrow 2) are strongly suppressed and only remnants of the
674 vortices are visible in the viscoelastic fluid. In the cloud cavitation region, vortices form
675 in the shear layer between the recirculating flow and the main flow, therefore they can
676 have large radial velocity components as the vorticity vector is likely to be located in the
677 cross-sectional plane of the nozzle (i.e. vortices rotating out of the cross sectional
678 plane). However in the string region the cavitating vortex is positioned in the
679 streamwise direction (vorticity vector in the axial direction). Therefore, as the polymers
680 tend to align with the main flow direction¹⁰² and suppress the cross flow fluctuations⁸⁷,
681 viscoelasticity tends to damp the vortices in the cloud region while stimulating the string
682 cavity vortex.

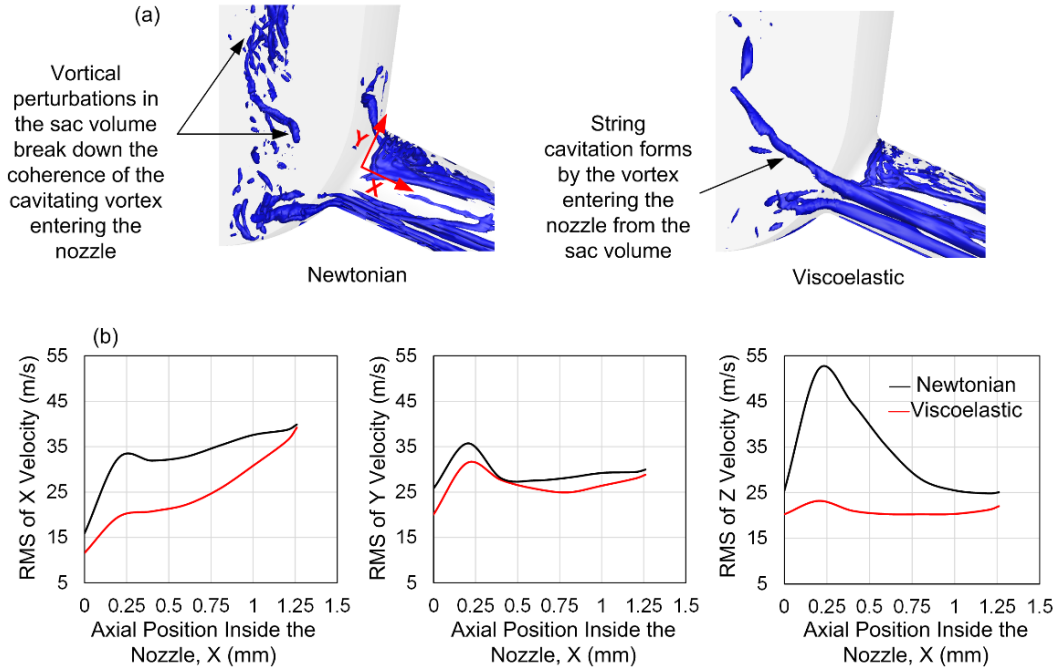


683

684 *Figure 12. (a) and (b) evaporation and condensations rates computed by the mass transfer rate*
 685 *cavitation model in the cloud and the string cavitation region, (c) vortical flow structures in the*
 686 *vicinity of the injector nozzle entrance plotted using the contours of second invariant of the*
 687 *velocity gradient (Q-criterion) in the nozzle mid-plane and translucent iso-surfaces of Q-criterion*
 688 *at $5E+12 \text{ s}^{-2}$*

689 As it was mentioned earlier, the vortex forming the string cavitation enters the nozzle
 690 from the sac volume and is formed by the swirling flow inside the sac volume ⁷⁰. Hence
 691 the level of turbulence upstream the nozzle entrance, can have a significant effect on
 692 the strength of the cavitating vortex. In Figure 13 (a) the flow structures in the sac
 693 volume in terms of the second invariant of the velocity gradient are displayed.
 694 Circumferential perturbations on the interface of a cavitating vortex can cause strong
 695 radial oscillations which result in splitting and collapse of the cavity core¹¹⁹. Moreover,
 696 flow instabilities upstream the vortex can cause the divergence of the stream tubes
 697 forming the vortex core, eventually breaking down the vortex ¹²⁰. The turbulent eddies
 698 in the sac volume in the Newtonian fluid (Figure 13 (a)) appear to breakdown the
 699 coherence of the vortex entering the nozzle. Furthermore, fluid elasticity can suppress

700 or delay the vortex breakdown as it prevents sharp velocity variations along the vortex
 701 centerline which initiate the breakdown process ¹²¹.



702

703 *Figure 13. (a) Vortex structures inside the sac volume visualized using the iso-surface of second invariant of*
 704 *the velocity gradient at $4E+12 s^{-2}$, (b) velocity fluctuations inside the nozzle plotted in terms of RMS of X, Y*
 705 *and Z velocity, values obtained from surface-averaged data calculated in slices along the nozzle*

706 The vortex disturbance inside the sac volume is significantly lower in the viscoelastic
 707 fluid compared to the Newtonian fluid in Figure 13 (a) and the large vortex entering the
 708 nozzle can be clearly identified. Reduction of vortex interactions in the sac volume
 709 contributes to stabilization of the cavitating vortex upstream of the nozzle entrance,
 710 which in turn allows a stronger string cavity to develop inside the nozzle. The
 711 fluctuations inside the nozzle in terms of RMS of the velocity components are plotted in
 712 Figure 13 (b). It is evident that due to the stabilizing effect of viscoelasticity on flow
 713 turbulence, all three components of velocity fluctuations are reduced in the viscoelastic
 714 fluid (by 23%, 9% and 31% in X, Y and Z directions respectively). This will therefore
 715 reduce the perturbations that destabilize the string cavity coherence inside the nozzle,
 716 allowing the cavitation structures to last longer.

717

718 **4. Conclusions**

719 In this study the effect of viscoelasticity on formation and development of cavitation
720 inside a step nozzle and an injector nozzle is studied in PTT fluids using the Schnerr-
721 Sauer cavitation model and the WALE turbulence model. In the step nozzle, incipient
722 cloud cavitation is forming whereas in the injector the cavitation cloud is fully developed
723 while a string cavitation is forming in the core of the vortex originating from the sac
724 volume.

725 In the step nozzle case, larger coherent structures become more dominant in the flow
726 as the smaller eddies are suppressed due to flow resistance to rotational motion in the
727 viscoelastic fluid. The dominant frequency of mass flowrate fluctuations is significantly
728 reduced from 168 Hz in the Newtonian fluid to 57 Hz in the viscoelastic fluid and higher
729 frequency (smaller amplitude) fluctuations are damped.

730 Moreover, fewer cavitating microvortices appear in the viscoelastic fluid and the
731 cavitation cloud structures are altered by viscoelasticity as large-scale cavitating
732 vortices appear stretched and enlarged compared to the Newtonian fluid. Time-
733 averaged statistics show that the vapor volume fraction is reduced more than 50% in
734 the viscoelastic fluid and the cavitation cloud is pushed away from the nozzle wall,
735 while the cloud thickness is reduced by more than 15%.

736 In the injector test case, the total vapor volume fraction is reduced in the viscoelastic
737 fluid by more than 40%, however there are significant differences in the effect of
738 viscoelasticity on the cloud cavitation and the string cavitation mechanisms. In the
739 cloud cavitation region, viscoelasticity reduces the vapor volume fraction, whereas in
740 the string cavitation region vapor volume fraction is enhanced. String cavitation forms
741 in the core of the quasi-streamwise vortex inside the nozzle and it is prone to
742 breakdown by velocity fluctuations upstream of the nozzle and inside the nozzle. The

743 cavitating vortex becomes more stable as viscoelasticity stimulates the longitudinal
744 vortices while suppressing the cross-stream fluctuations inside the nozzle and reducing
745 the vortical perturbations in the sac volume. However as vortices in the cloud region
746 rotate out of the cross-sectional plane (vorticity vector positioned in the cross-flow
747 direction), they are damped by viscoelasticity.

748 Further experimental and numerical investigations on viscoelastic cavitating flows are
749 important for addressing the underlying mechanisms involved in this type of flow.

750 Interface capturing methods and modelling of subgrid scale viscoelastic effects as well
751 as PIV-LIF and X-ray techniques can provide valuable data for understanding the of
752 flow physics and validation of computational studies.

753

754

755

756 **Acknowledgments**

757 This work has received financial support from City, University of London and Lubrizol
758 Ltd UK. The authors also acknowledge the contribution of The Lloyd's Register
759 Foundation. Lloyd's Register Foundation helps to protect life and property by
760 supporting engineering-related education, public engagement and the application of
761 research. The authors would also like to thank Dr. Ioannis Karathanassis for the
762 valuable discussions during the preparation of this manuscript.

763

764

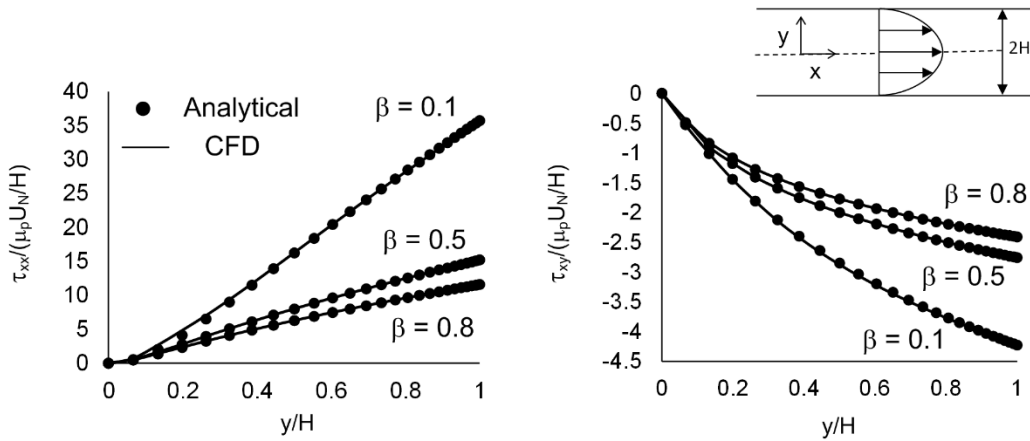
765

766 **Competing financial statement:**

767 The authors declare no competing financial interests.

768 **Appendix A: Viscoelastic code validation**

769 Calculations performed with the viscoelastic model are compared against the analytical
 770 solution for the fully developed channel flow of the PTT fluid ¹²². The tangential and
 771 normal components of the stress are calculated for various β values (ratio of solvent to
 772 total viscosity) and the relaxation time is chosen such that Deborah number ($De =$
 773 $\lambda U/H$, where U and H are characteristic velocity and length scales of flow) is equal to
 774 1. Tangential and normal stress components are non-dimensionalized by the stress
 775 scale $\mu_p U_N/H$, where H is the channel half-height and U_N is a velocity scale defined as
 776 $U_N = -p_z H^2/8\mu_0$ and p_z is the pressure gradient across the channel. The stress values
 777 predicted by the code match the analytical calculations.



778
 779 *Figure 14. Comparison of the CFD code and the analytical solution for the PTT model, non-*
 780 *dimensionalized normal viscoelastic stresses (left) and tangential viscoelastic stresses (right) in*
 781 *the channel at different viscosity ratios ($\beta = \mu_s / \mu_0$) are compared for $\epsilon = 0.25$ and $De = 1$*

782 This graph shows that by increasing the polymer strength (lower β values), the stresses
 783 are higher in both normal and tangential directions. Moreover in the centerline ($y/H =$
 784 0), stresses are zero because in the fully developed flow, the velocity gradient
 785 approaches zero near the center of the channel. Also as expected, maximum stress
 786 values occur at the contact with the wall where the velocity gradient and shear stresses
 787 are maximum.

788 **References**

- 789 1. Tan, D. *et al.* Experimental Investigation of the Role of Large Scale Cavitating Vortical
790 Structures in Performance Breakdown of an Axial Waterjet Pump. *J. Fluids Eng.* **137**,
791 111301 (2015).
- 792 2. Dreyer, M., Decaix, J., Münch-alligné, C. & Farhat, M. Mind the gap: a new insight into
793 the tip leakage vortex using stereo-PIV. *Exp Fluids* **55**, 1849 (2014).
- 794 3. Arndt, R., Pennings, P., Bosschers, J. & Van Terwisga, T. The singing vortex. *Interface*
795 *Focus* **5**, 1–11 (2015).
- 796 4. Egerer, C. P., Hickel, S., Schmidt, S. J. & Adams, N. A. Large-eddy simulation of
797 turbulent cavitating flow in a micro channel. *Phys. Fluids* **26**, 85102 (2014).
- 798 5. Hickel, S. DNS and LES of two-phase flows with cavitation. *Direct Large-Eddy Simul.* **IX**,
799 595–604 (2015).
- 800 6. Koukouvinis, P., Mitroglou, N., Gavaises, M., Lorenzi, M. & Santini, M. Quantitative
801 predictions of cavitation presence and erosion-prone locations in a high-pressure
802 cavitation test rig. *J. Fluid Mech.* **819**, 21–57 (2017).
- 803 7. Song, J. H., Johansen, K. & Prentice, P. Covert cavitation: Spectral peak suppression in
804 the acoustic emissions from spatially configured nucleations. *J. Acoust. Soc. Am.* **141**,
805 216 (2017).
- 806 8. Lu, Y., Katz, J. & Prosperetti, A. Dynamics of cavitation clouds within a high-intensity
807 focused ultrasonic beam. *Phys. Fluids* **25**, (2013).
- 808 9. Macoskey, J. J. *et al.* Bubble-Induced Color Doppler Feedback Correlates with
809 Histotripsy-Induced Destruction of Structural Components in Liver Tissue. *Ultrasound*
810 *Med. Biol.* **44**, 602–612 (2018).
- 811 10. Bergwerk, W. FLOW PATTERN IN DIESEL NOZZLE SPRAY HOLES. *Proc. Inst. Mech.*
812 *Eng.* **173**, 655–660 (1959).

- 813 11. Schmidt, D. P. & Corradini, M. L. The internal flow of diesel fuel injector nozzles: a
814 review. *Int. J. Engine Res.* **2**, 1–22 (2001).
- 815 12. Som, S., Aggarwal, S. K., El-Hannouny, E. M. & Longman, D. E. Investigation of Nozzle
816 Flow and Cavitation Characteristics in a Diesel Injector. *J. Eng. Gas Turbines Power*
817 **132**, 42802 (2010).
- 818 13. Duke, D. J., Kastengren, A. L., Tilocco, F. Z., Swantek, A. B. & Powell, C. F. X-RAY
819 RADIOGRAPHY MEASUREMENTS OF CAVITATING NOZZLE FLOW. *At. Sprays* **23**,
820 841–860 (2013).
- 821 14. Giannadakis, E., Gavaises, M. & Arcoumanis, C. Modelling of cavitation in diesel injector
822 nozzles. *J. Fluid Mech.* **616**, 153–193 (2008).
- 823 15. Kastengren, A. L. *et al.* TIME-RESOLVED X-RAY RADIOGRAPHY OF SPRAYS FROM
824 ENGINE COMBUSTION NETWORK SPRAY A DIESEL INJECTORS. *At. Sprays* **24**,
825 251–272 (2014).
- 826 16. Mitroglou, N., Lorenzi, M., Santini, M. & Gavaises, M. Application of X-ray micro-
827 computed tomography on high-speed cavitating diesel fuel flows. *Exp. Fluids* **57**, 175
828 (2016).
- 829 17. Örley, F. *et al.* Large-eddy simulation of cavitating nozzle flow and primary jet break-up.
830 *Phys. Fluids* **27**, 86101 (2015).
- 831 18. Gopalan, S. & Katz, J. Flow structure and modeling issues in the closure region of
832 attached cavitation. *Phys. Fluids* **12**, 895–911 (2000).
- 833 19. Iyer, C. O. & Ceccio, S. L. The influence of developed cavitation on the flow of a
834 turbulent shear layer. *Phys. Fluids* **14**, 3414–3431 (2002).
- 835 20. Dittakavi, N., Chuneekar, A. & Frankel, S. Large Eddy Simulation of Turbulent-Cavitation
836 Interactions in a Venturi Nozzle. *J. Fluids Eng.* **132**, 121301 (2010).
- 837 21. Aeschlimann, V., Barre, S. & Djeridi, H. Velocity field analysis in an experimental
838 cavitating mixing layer. *Phys. Fluids* **23**, 55105 (2011).

- 839 22. Ganesh, H., Makiharju, S., Ceccio, S. & Ganesh, H. Bubbly shock propagation as a
840 mechanism for sheet-to-cloud transition of partial cavities. *J. Fluid Mech* **802**, 37–78
841 (2016).
- 842 23. Karathanassis, I. K. *et al.* High-speed visualization of vortical cavitation using
843 synchrotron radiation. *J. Fluid Mech* **838**, 148–164 (2018).
- 844 24. Sridhar, G. & Katz, J. Effect of entrained bubbles on the structure of vortex rings. *J. Fluid*
845 *Mech.* **397**, 171–202 (1999).
- 846 25. Ceccio, S. L. Friction Drag Reduction of External Flows with Bubble and Gas Injection.
847 *Annu. Rev. Fluid Mech* **42**, 183–203 (2010).
- 848 26. Ferrante, A. & Elghobashi, S. Reynolds number effect on drag reduction in a
849 microbubble-laden spatially developing turbulent boundary layer. *J. Fluid Mech* **543**, 93–
850 106 (2005).
- 851 27. Sugiyama, K., Calzavarini, E. & Lohse, D. Microbubbly drag reduction in Taylor-Couette
852 flow in the wavy vortex regime. *J. Fluid Mech.* **608**, 21–41 (2008).
- 853 28. Kawakami, E. & Arndt, R. E. A. Investigation of the Behavior of Ventilated Supercavities.
854 *J. Fluids Eng.* **133**, 91305 (2011).
- 855 29. Karn, A. *et al.* An experimental investigation into supercavity closure mechanisms. *J.*
856 *Fluid Mech* **789**, 259–284 (2016).
- 857 30. Mäkiharju, S. A., Ganesh, H. & Ceccio, S. L. The dynamics of partial cavity formation,
858 shedding and the influence of dissolved and injected non-condensable gas. *J. Fluid*
859 *Mech* **829**, 420–458 (2017).
- 860 31. Legner, H. H. A simple model for gas bubble drag reduction. *Phys. Fluids* **27**, 2788
861 (1984).
- 862 32. Llewellyn, E. W. *et al.* The Rheology of a Bubbly Liquid. *Source Proc. Math. Phys. Eng.*
863 *Sci.* **458**, 987–1016 (2001).

- 864 33. Toms, B. A. Some observations on the flow of linear polymer solutions through straight
865 tubes at large Reynolds numbers. in *Proceedings of the 1st International Congress on*
866 *Rheology* (1948).
- 867 34. Virk, P. S. An elastic sublayer model for drag reduction by dilute solutions of linear
868 macromolecules. *J. Fluid Mech.* **45**, 417–440 (1971).
- 869 35. Virk, P. S. Drag reduction fundamentals. *AIChE J.* **21**, 625–656 (1975).
- 870 36. Ohlendorf, D., Interthal, W. & Hoffmann, H. Surfactant systems for drag reduction:
871 Physico-chemical properties and rheological behaviour. *Rheol. Acta* **25**, 468–486 (1986).
- 872 37. Bewersdorff, H.-W. & Ohlendorf, D. The behaviour of drag-reducing cationic surfactant
873 solutions. *Colloid Polym. Sci.* **266**, 941–953 (1988).
- 874 38. Luchik, T. S. & Tiederman, W. G. Turbulent structure in low-concentration drag-reducing
875 channel flows. *J. Fluid Mech.* **190**, 241–263 (1988).
- 876 39. Dimitropoulos, C. D., Sureshkumar, R. & Beris, A. N. Direct numerical simulation of
877 viscoelastic turbulent channel flow exhibiting drag reduction: effect of the variation of
878 rheological parameters. *J. Nonnewton. Fluid Mech.* **79**, 433–468 (1998).
- 879 40. Li, F.-C., Kawaguchi, Y. & Hishida, K. Investigation on the characteristics of turbulence
880 transport for momentum and heat in a drag - reducing surfactant solution flow. *Phys.*
881 *Fluids* **16**, 3281–3295 (2004).
- 882 41. Dimitropoulos, C. D., Dubief, Y., Shaqfeh, E. S. G., Moin, P. & Lele, S. K. Direct
883 numerical simulation of polymer-induced drag reduction in turbulent boundary layer flow.
884 *Phys. Fluids* **17**, 11705 (2005).
- 885 42. Dubief, Y. *et al.* On the coherent drag-reducing and turbulence-enhancing behaviour of
886 polymers in wall flows. *J. Fluid Mech.* **514**, 271–280 (2004).
- 887 43. White, C. M. & Mungal, M. G. Mechanics and prediction of turbulent drag reduction with
888 polymer additives. *Annu. Rev. Fluid Mech.* **40**, 235–256 (2008).

- 889 44. Procaccia, I., L'vov, V. S. & Benzi, R. Colloquium: Theory of drag reduction by polymers
890 in wall-bounded turbulence. *Rev. Mod. Phys.* **80**, 225–247 (2008).
- 891 45. Xi, L. & Graham, M. Turbulent drag reduction and multistage transitions in viscoelastic
892 minimal flow units. *J. Fluid Mech.* **647**, 421–452 (2010).
- 893 46. Graham, M. D. Drag reduction and the dynamics of turbulence in simple and complex
894 fluids. *Phys. Fluids* **26**, 101301–24 (2014).
- 895 47. Japper-Jaafar, A., Escudier, M. P. & Poole, R. J. Laminar, transitional and turbulent
896 annular flow of drag-reducing polymer solutions. *J. Non-Newtonian Fluid Mech* **165**,
897 1357–1372 (2010).
- 898 48. Owolabi, B. E., Dennis, D. J. C. & Poole, R. J. Turbulent drag reduction by polymer
899 additives in parallel-shear flows. *J. Fluid Mech* **827**, R4 (2017).
- 900 49. Li, C.-F., Sureshkumar, R. & Khomami, B. Influence of rheological parameters on
901 polymer induced turbulent drag reduction. *J. Nonnewton. Fluid Mech.* **140**, 23–40 (2006).
- 902 50. Rose, G. D. & Foster, K. L. Drag reduction and rheological properties of cationic
903 viscoelastic surfactant formulations. *J. Nonnewton. Fluid Mech.* **31**, 59–85 (1989).
- 904 51. Zakin, J. L., Lu, B. & Bewersdorff, H.-W. Surfactant drag reduction. *Rev. Chem. Eng.* **14**,
905 253–320 (1998).
- 906 52. *Wormlike Micelles: Advances in Systems, Characterisation and Applications*. (Royal
907 Society of Chemistry, 2017). doi:10.1039/9781782629788
- 908 53. Lumley, J. L. Drag reduction in turbulent flow by polymer additives. *J. Polym. Sci.*
909 *Macromol. Rev.* **7**, 263–290 (1973).
- 910 54. Ryskin, G. Turbulent Drag Reduction by Polymers: A Quantitative Theory. *Phys. Rev.*
911 *Lett.* **59**, 2059–2062 (1987).
- 912 55. L'vov, V. S., Pomyalov, A., Procaccia, I. & Tiberkevich, V. Drag Reduction by Polymers
913 in Wall Bounded Turbulence. *Phys. Rev. Lett.* **92**, 244503 (2004).

- 914 56. Tabor, M. & de Gennes, P. G. A Cascade Theory of Drag Reduction. *Europhys. Lett.* **2**,
915 519–522 (1986).
- 916 57. Goldberg, B. B., Liu, J.-B. & Forsberg, F. ULTRASOUND CONTRAST AGENTS: A
917 REVIEW. *Ultrasound Med. Biol.* **20**, 319–333 (1994).
- 918 58. Roberts, W. W. *et al.* Pulsed Cavitation Ultrasound: A Noninvasive Technology for
919 Controlled Tissue Ablation (Histotripsy) in the Rabbit Kidney. *J. Urol.* **175**, 734–738
920 (2006).
- 921 59. Brujan, E. A., Ohi, C. D., Lauterborn, W. & Philipp, A. Dynamics of laser-induced
922 cavitation bubbles in polymer solutions. *Acta Acust. united with Acust.* **82**, 423–430
923 (1996).
- 924 60. Chahine, G. L. & Fruman, D. H. Dilute polymer solution effects on bubble growth and
925 collapse. *Phys. Fluids* **22**, 1406 (1979).
- 926 61. Brujan, E. A., Ikeda, T. & Matsumoto, Y. Dynamics of ultrasound - induced cavitation
927 bubbles in non - Newtonian liquids and near a rigid boundary. *Phys. Fluids* **16**, 2402–
928 2410 (2004).
- 929 62. Lind, S. J. & Phillips, T. N. The influence of viscoelasticity on the collapse of cavitation
930 bubbles near a rigid boundary. *Theor. Comput. Fluid Dyn.* **26**, 245–277 (2012).
- 931 63. Lind, S. J. & Phillips, T. N. Bubble Collapse in Compressible Fluids using a Spectral
932 Element Marker Particle Method. Part 2. Viscoelastic Fluids. *Int. J. Numer. Meth. Fluids*
933 **71**, 1103–1130 (2013).
- 934 64. Brujan, E.-A. Shock wave emission from laser-induced cavitation bubbles in polymer
935 solutions. *Ultrasonics* **48**, 423–426 (2008).
- 936 65. Hua, C. & Johnsen, E. Nonlinear oscillations following the Rayleigh collapse of a gas
937 bubble in a linear viscoelastic (tissue-like) medium. *Phys. Fluids* **25**, 83101 (2013).
- 938 66. Warnez, M. T. & Johnsen, E. Numerical modeling of bubble dynamics in viscoelastic
939 media with relaxation. *Phys. Fluids* **27**, 63103 (2015).

- 940 67. Jiménez-Fernández, J. & Crespo, A. Bubble oscillation and inertial cavitation in
941 viscoelastic fluids. *Ultrasonics* **43**, 643–651 (2005).
- 942 68. Brennen, C. E. *Cavitation and Bubble Dynamics*. (Cambridge University Press, 2013).
- 943 69. Andriotis, A., Gavaises, M. & Arcoumanis, C. Vortex flow and cavitation in diesel injector
944 nozzles. *J. Fluid Mech.* **610**, 195–215 (2008).
- 945 70. Gavaises, M., Andriotis, A., Papoulias, D., Mitroglou, N. & Theodorakakos, A.
946 Characterization of string cavitation in large-scale Diesel nozzles with tapered holes.
947 *Phys. Fluids* **21**, 52107–52107 (2009).
- 948 71. Callenaere, M., Franc, J., Michel, J. & Riondet, M. The cavitation instability induced by
949 the development of a re-entrant jet. *J. Fluid Mech* **444**, 223–256 (2001).
- 950 72. Chahine, G. L., Frederick, G. F. & Bateman, R. D. Propeller Tip Vortex Cavitation
951 Suppression Using Selective Polymer Injection. *J. Fluids Eng.* **115**, 497–503 (1993).
- 952 73. Chang, N., Ganesh, H., Yakushiji, R. & Ceccio, S. L. Tip Vortex Cavitation Suppression
953 by Active Mass Injection. *J. Fluids Eng.* **133**, 111301 (2011).
- 954 74. Thien, N. P. & Tanner, R. I. A new constitutive equation derived from network theory. *J.*
955 *Nonnewton. Fluid Mech.* **2**, 353–365 (1977).
- 956 75. Poole, R. J., Escudier, M. P., Afonso, A. & Pinho, F. T. Laminar flow of a viscoelastic
957 shear-thinning liquid over a backward-facing step preceded by a gradual contraction.
958 *Phys. Fluids* **19**, 1–17 (2007).
- 959 76. Afonso, A. & Pinho, F. T. Numerical investigation of the velocity overshoots in the flow of
960 viscoelastic fluids inside a smooth contraction. *J. Nonnewton. Fluid Mech.* **139**, 1–20
961 (2006).
- 962 77. Nicoud, F. & Ducros, F. Subgrid-scale stress modelling based on the square of the
963 velocity gradient tensor. *Flow, Turbul. Combust.* **62**, 183–200 (1999).
- 964 78. Schnerr, G. H. & Sauer, J. Physical and numerical modeling of unsteady cavitation

- 965 dynamics. in *Fourth International Conference on Multiphase Flow* (2001).
- 966 79. Franc, J.-P. & Michel, J.-M. *Fundamentals of Cavitation*. (Springer Netherlands, 2005).
967 doi:10.1007/1-4020-2233-6
- 968 80. Sibley, D. N. *Viscoelastic Flows of PTT Fluids*. (University of Bath, 2010).
- 969 81. Jasak, H., Weller, H. G. & Gosman, A. A. D. HIGH RESOLUTION NVD DIFFERENCING
970 SCHEME FOR ARBITRARILY UNSTRUCTURED MESHES. *Int. J. Numer. Meth. Fluids*
971 **31**, 431–449 (1999).
- 972 82. Sureshkumar, R. & Beris, A. N. Effect of artificial stress diffusivity on the stability of
973 numerical calculations and the flow dynamics of time-dependent viscoelastic flows. *J.*
974 *Nonnewton. Fluid Mech.* **60**, 53–80 (1995).
- 975 83. Issa, R. I. Solution of the Implicitly Discretised Fluid Flow Equations by Operator-
976 Splitting. *J. Comput. Phys.* **62**, 40–65 (1985).
- 977 84. Chen, Z. J. & Przekwas, A. J. A coupled pressure-based computational method for
978 incompressible/compressible flows. *J. Comput. Phys.* **229**, 9150–9165 (2010).
- 979 85. Giudice, F. Del, Haward, S. J. & Shen, A. Q. Relaxation time of dilute polymer solutions:
980 A microfluidic approach. *J. Rheol. (N. Y. N. Y.)* **61**, 327–337 (2017).
- 981 86. Valente, P. C., Da Silva, C. B. & Pinho, F. T. The effect of viscoelasticity on the turbulent
982 kinetic energy cascade. *J. Fluid Mech* **760**, 39–62 (2014).
- 983 87. Yu, B., Li, F. & Kawaguchi, Y. Numerical and experimental investigation of turbulent
984 characteristics in a drag-reducing flow with surfactant additives. *Int. J. heat fluid flow* **25**,
985 961–974 (2004).
- 986 88. Sou, A., Biçer, B. & Tomiyama, A. Numerical simulation of incipient cavitation flow in a
987 nozzle of fuel injector. *Comput. Fluids* **103**, 42–48 (2014).
- 988 89. Koukouvinis, Naseri, H. & Gavaises, M. Performance of turbulence and cavitation
989 models in prediction of incipient and developed cavitation. *Int. J. Engine Res.* **18**, 333–

- 990 350 (2016).
- 991 90. Addad, Y., Gaitonde, U., Laurence, D. & Rolfo, S. in *In: J. Meyers, B.J. Geurts, P.*
992 *Sagaut (eds) Quality and Reliability of Large-Eddy Simulations. Ercoftac Series 12*, 93–
993 103 (Springer, Dordrecht, 2008).
- 994 91. Howard, R. J. A. & Pourquie, M. Large eddy simulation of an Ahmed reference model. *J.*
995 *Turbul.* **3**, (2002).
- 996 92. Lesieur, M., Métais, O. & Comte, P. *Large-eddy simulations of turbulence*. (Cambridge
997 University Press, 2005).
- 998 93. Lesieur, M. *Turbulence in Fluids*. (Springer Science & Business Media, 2012).
- 999 94. Tennekes, H. & Lumley, J. L. *A first course in turbulence*. (MIT Press, 1972).
- 1000 95. Örley, F., Hickel, S., Schmidt, S. J. & Adams, N. A. Large-Eddy Simulation of turbulent,
1001 cavitating fuel flow inside a 9-hole Diesel injector including needle movement. *Int. J.*
1002 *Engine Res.* **18**, 195–211 (2017).
- 1003 96. Kolev, N. I. *Multiphase Flow Dynamics*. (Springer, 2005).
- 1004 97. Richter, D., Iaccarino, G. & Shaqfeh, E. S. G. Effects of viscoelasticity in the high
1005 Reynolds number cylinder wake. *J. Fluid Mech.* **693**, 297–318 (2012).
- 1006 98. Haller, G. An objective definition of a vortex. *J. Fluid Mech.* **525**, 1–26 (2005).
- 1007 99. Cadot, O. & Lebey, M. Shear instability inhibition in a cylinder wake by local injection of a
1008 viscoelastic fluid. *Phys. Fluids* **11**, 494–496 (1999).
- 1009 100. Lin, J., Yu, Z. & Shao, X. Coherent structures in the mixing layers of a non-Newtonian
1010 fluid. *J. Turbul.* **5**, 39 (2004).
- 1011 101. Pereira, A. S., Mompean, G., Thais, L. & Soares, E. J. Transient aspects of drag
1012 reducing plane Couette flows. *J. Nonnewton. Fluid Mech.* **241**, 60–69 (2017).
- 1013 102. Pereira, A. S., Mompean, G., Thais, L. & Thompson, R. L. Statistics and tensor analysis
1014 of polymer coil-stretch mechanism in turbulent drag reducing channel flow. *J. Fluid*

- 1015 *Mech.* **824**, 135–173 (2017).
- 1016 103. Seyer, F. A. & Metzner, A. B. Turbulence phenomena in drag reducing systems. *AIChE*
1017 *J.* **15**, 426–434 (1969).
- 1018 104. Housiadas, K. D. & Beris, A. N. Direct numerical simulations of viscoelastic turbulent
1019 channel flows at high drag reduction. *Korea - Aust. Rheol. J.* **17**, 131–140 (2005).
- 1020 105. Xie, Y.-C. *et al.* Effects of polymer additives in the bulk of turbulent thermal convection. *J*
1021 *. Fluid Mech* **784**, R3 (2015).
- 1022 106. Valente, P. C., da Silva, C. B. & Pinho, F. T. Energy spectra in elasto-inertial turbulence.
1023 *Phys. Fluids* **28**, 75108 (2016).
- 1024 107. Soldati, A. & Banerjee, S. Turbulence modification by large-scale organized
1025 electrohydrodynamic flows. *Phys. Fluids* **10**, 1742–1756 (1998).
- 1026 108. Pelz, P. F. *et al.* in *Advanced Experimental and Numerical Techniques for Cavitation*
1027 *Erosion Prediction* (eds. Kim K., Chahine G., Franc J. P. & Karimi A.) (2014).
1028 doi:10.1007/978-94-017-8539
- 1029 109. Hegedús, F., Hós, C., Pandula, Z. & Kullmann, L. Measurement on the cavitating vortex
1030 shedding behind rectangular obstacles. *IOP Conf. Ser. Earth Environ. Sci.* **12**, 12066
1031 (2010).
- 1032 110. Kim, B. K. & Telionis, D. P. The effect of polymer additives on laminar separation. *Phys.*
1033 *Fluids A Fluid Dyn.* **1**, 267–273 (1989).
- 1034 111. Oliveira, P. J. Method for time-dependent simulations of viscoelastic flows: vortex
1035 shedding behind cylinder. *J. Nonnewton. Fluid Mech.* **101**, 113–137 (2001).
- 1036 112. Norouzi, M., Varedi, S. R. & Zamani, M. Wake instability of viscoelastic flows past an
1037 unconfined inclined square cylinder. *Phys. Fluids* **28**, 23101 (2016).
- 1038 113. Sureskumar, R., Beris, A. N. & Handler, A. H. Direct numerical simulation of the turbulent
1039 channel flow of a polymer solution. *Phys. Fluids* **9**, 743–755 (1997).

- 1040 114. Afzal, H., Arcoumanis, C., Gavaises, M. & Kampanis, N. Internal flow in diesel injector
1041 nozzles: modelling and experiments. *IMechE Pap.* S 25–44 (1999).
- 1042 115. Duke, D. *et al.* X-ray imaging of cavitation in Diesel injectors. *SAE Int. J. Engines* **7**,
1043 1003–1016 (2014).
- 1044 116. DEGANI, D., SEGINER, A. & LEVY, Y. Graphical visualization of vortical flows by means
1045 of helicity. *AIAA J.* **28**, 1347–1352 (1990).
- 1046 117. Tsukahara, T., Motozawa, M. & Tsurumi, D. PIV and DNS analyses of viscoelastic
1047 turbulent flows behind a rectangular orifice. *Int. J. Heat Fluid Flow* 66–79 (2013).
- 1048 118. Kim, K., Adrian, R. J., Balachandar, S. & Sureshkumar, R. Dynamics of Hairpin Vortices
1049 and Polymer-Induced Turbulent Drag Reduction. *Phys. Rev. Lett.* **100**, 134504 (2008).
- 1050 119. Choi, J., Hsaio, C., Chahine, G. & Ceccio, S. Growth, oscillation and collapse of vortex
1051 cavitation bubbles. *J. Fluid Mech.* **624**, 255–279 (2009).
- 1052 120. Hall, M. G. VORTEX BREAKDOWN. *Annu. Rev. Fluid Mech.* **4**, 195–318 (1972).
- 1053 121. Stokes, J. R., W Graham, L. J., Lawson, N. J. & Boger, D. V. Swirling flow of viscoelastic
1054 fluids. Part 1. Interaction between inertia and elasticity. *J. Fluid Mech* **429**, 67–115
1055 (2001).
- 1056 122. Cruz, D. O. A., Pinho, F. T. & Oliveira, P. J. Analytical solutions for fully developed
1057 laminar flow of some viscoelastic liquids with a Newtonian solvent contribution. *J.*
1058 *Nonnewton. Fluid Mech.* **132**, 28–35 (2005).
- 1059
- 1060